Electronic Supporting Information:

Thermally processed Ni-and Co-struvites as functional materials for proton conductivity

Stephanos Karafiludis[1,2*], Biswajit Bhattacharya[1], Ana Guilherme Buzanich[1], Friedrich Fink[1], Ines Feldmann[1], Johan E. ten Elshof[3], Franziska Emmerling[1,2] and Tomasz M. Stawski[1*]

[1]Federal Institute for Materials Research and Testing, Unter den Eichen 87, 12205 Berlin, Germany

[2]Department of Chemistry, Humboldt-Universität zu Berlin, Brook-Taylor-Straße 2, 12489 Berlin, Germany

[3]MESA+ Institute for Nanotechnology, University of Twente, P.O. Box 217, 7500 AE Enschede, the Netherlands

Stephanos Karafiludis: https://orcid.org/0000-0002-7257-6311;
Biswajit Bhattacharya: https://orcid.org/0000-0003-4138-1287 ;
Ana Guilherme Buzanich: https://orcid.org/0000-0001-5543-9924;
Friedrich Fink: https://orcid.org/0000-0002-9439-2871;
Ines Feldmann: https://orcid.org/0000-0003-2650-9270;
Johan E. ten Elshof: https://orcid.org/0000-0001-7995-6571 ;
Franziska Emmerling: https://orcid.org/0000-0001-8528-0301;
Tomasz M. Stawski: https://orcid.org/0000-0002-0881-5808;
Corresponding authors: *tomasz.stawski@bam.de ;* stephanos.karafiludis@bam.de

List of Contents

List of Figures

List of Tables

Methods

X-ray diffraction

Powder X-ray diffraction (PXRD, XRD) measurements from the powders were performed on a D8 Bruker Diffractometer equipped with a LYNXEYE XE-T detector. The diffraction data were collected with Cu Kα radiation (1.5406 Å, 40 kV and 40 mA) from 5-60° using a step size 0.015° (2Θ) and a scanning time of 0.5 s per step. All samples were prepared on silicon specimen holders in order to minimize background especially important in the case of the amorphous phases.

SEM

The scanning electron microscopy (SEM) analysis was performed on an XL 30 ESEM equipped with a tungsten cathode (FEI, Eindhoven, in 2020 electronic upgrade by point electronic GmbH) operating with a 20 keV acceleration voltage and using a secondary electron detector (SE). Before the analysis, all samples were coated with a 30 nm thick layer of gold.

TGA/DSC

Thermal gravimetric analysis (TGA) and differential scanning calorimetry (DSC) were performed simultaneously on dry M-struvite powders using a heat flux TGA/DSC 3+ device from Mettler Toledo. All measurements were carried out in a nitrogen atmosphere with a purge gas flow of 100 ml min^{-1}. As a reference material for the heat flux, DSC an α-Al_2O_3 corundum crucible, was used. All samples were heated from room temperature to 850 °C with a heating rate of 10 °C min^{-1}.

Infrared spectroscopy

FT-IR analysis was performed on a Nicolet Nexus 670 FT-IP (Thermo Fischer Scientific) in attenuated total reflection (ATR) mode with a "Golden Gate" sample holder, to track majorly the water and ammonia compounds in the samples. Before each measurement, the sample holder was cleaned with ethanol and acetone. Air was measured, as a background spectrum. 32 scans were taken with a resolution of 4 cm^{-1} per one sample measurement. The spectral range was set to 4000 – 570 cm^{-1} and the spectra were recorded in an absorption mode. The software OMNIC was used for acquisition and the spectra were exported in a CSV file format.

Raman spectroscopy

The Raman spectra were obtained on Labram HR 800 Raman microscope system from Horiba Jobin Yvon equipped with a BX41 microscope from Olympus. All data were processed by using the Horiba's LabSpec 6 software. All measurements were carried out with a continuous diode-pumped solid-state laser with a wavelength of λ = 532 nm resulting in power on the sample of 34 mW. A long-working distance 50x/N.A. = 0.55 microscope objective and a spectrometer grating with 1800 grooves mm^{-1} was used. The dry powdered samples were flattened on a microscope slide and the focus was set in a light microscopy mode. Afterwards, the laser was turned on, excited the sample and multiple point measurements from the sample were measured. In general, the acquisition parameters were 60 s measurement time per spectrum with five accumulations, but settings were also varied depending on the sample to avoid saturation effects. The centre wavenumber of the spectrum was around 1780 cm^{-1} with an entire range of 187-3387 cm^{-1} to see phosphate, water and ammonia vibrations.

X-ray absorption spectroscopy

XAS (X-ray absorption spectroscopy) measurements of the solid powders both at the near-edge structure (XANES) and extended fine structure (EXAFS) to resolve the coordination environment of the different phases, were performed at the BAMline (BESSY-II, Helmholtz Centre Berlin for Materials and Energy Berlin, Germany) [1] . The beam was monochromatized using a double-crystal monochromator (DCM) with a Si crystallographic orientation of [111]. The size of the beam was 3 mm (v) x 1 mm (h). The measurements were performed at the Ni-K edge (8333 eV) in transmission geometry, with two

ionization chambers as detectors. The excitation energy was varied from 8230 eV to 9302 eV for Ni, with varying energy steps. For the pre-edge region, the energy was varied in 10 eV steps; for the region around the edge, energy was tuned first in 0.5 eV steps, then in 1 eV steps (XANES) and in the EXAFS region with a constant step in the k-space of 0.04 $Å^{-1}$ until k = 16 Å. The associated uncertainties were experimentally determined by measuring the nickel metal foil, each 10 times. A value of ±0.3 eV was obtained for both systems. For the measurement, the samples were mixed with boron nitride, placed in polycarbonate hole plates with a thickness of 1 mm and sealed with a polyimide tape (Kapton) on both sides. Before collecting the sample spectra, a nickel foil was used as a reference for the respective K edge. The relative energies of the spectra were calibrated to the first infliction point of the nickel metal absorption edge.

The resulting XAS data were processed by using ATHENA (for normalization and background removal) and ARTEMIS (to fit known models to the experimental EXAFS data). These two programs belong to the main package IFEFFIT (v. 1.2.11) [2]. The respective Ni-phosphates (Ni-struvite $NH_4NiPO_4 \cdot 6H_2O$, Ni-dittmarite $NH_4NiPO_4 \cdot H_2O$ and Ni-pyrophosphate $Ni_2P_2O_7$) and Co-phosphates (Co-struvite $NH_4CoPO_4 \cdot 6H_2O$, Co-dittmarite $NH_4CoPO_4 \cdot H_2O$, hydrogencobaltphosphate monohydrate $HCoPO_4 \cdot H_2O$, anhydrous ammoniumcobaltphosphate NH_4CoPO_4 and Co-pyrophosphate $Co_2P_2O_7$) were used as model structures and the scattering paths for the first and second coordination sphere were theoretically modelled and fitted to the measured spectra using ARTEMIS.

Proton conductivity measurements

Proton conductivity (PC) properties were derived by performing alternating-current (AC) impedance measurements using an impedance and gain-phase analyzer (Biologic SP-150e) over a frequency range from 10 mHz to 1 MHz with an input voltage amplitude of 10 mV. Powder samples were pelletized under a pressure of 4.9 MPa for 5 min. Each pellet was coated with a silver paste on both sides and dried in the air overnight. Selected Ni- and Co-phosphate samples, thermally treated at temperatures from 25°C-800°C, were analyzed. All pellets dimension data and PC results are summarized in this SI. The corresponding proton conductivities of all three compounds were measured by inserting the pellet into a custom-made stainless-steel cell with the two-electrode setup (SI: Figure S1). The measurements were carried out over an extensive range of temperatures (25–80 °C) at a constant relative humidity (98%) and relative humidity levels (68–98% RH) at a constant temperature (25°C). The programmable Binder climate-controlled chamber (Model KMF) was used to keep the sample at the desired temperature and the relative humidity during a proton conductivity measurement. The conditions in the chamber for each measurement were allowed to equilibrate for 12 hours.

Impedance spectra were fitted with a minimal circuit model with the software *EIS Spectrum Analyser (Version 07/2013)*[3]. Our equivalent circuit model (Fig. 5B in the main text) comprises a constant-phase element (CPE) and a resistor (R) in parallel connected in series with two parallel Warburg elements (short and open Warburg elements W_S and W_O). Here, the Warburg short and open element can account for semi-finite to finite diffusion of protons as they represent the transmissive and reflective character of the grain boundaries, respectively. The high-frequency R-CPE circuit represents the electronic resistivity of the metal phosphate phase. The proton conductivities were calculated from the intersection of the fits in the Nyquist plots with the abscissa axis (real part of impedance Z'). Proton conductivity values were calculated using the following equation (Equation S1):

$$\sigma = \frac{l}{AZ'} \qquad [S1]$$

where l is the distance between the electrodes i.e., the thickness of the pellet and A is the cross section area of the pellet. Z' is the through-plane bulk impedance of the sample. Since the other measured

samples (T = 300°C, 500°C and 800°C) changed their chemical composition and structure, only the intersection of the semicircles in the Nyquist plots with the abscissa axis was used for comparison. Here an interpretation of a fitting circuit would be misleading because multiple reactions occur, and assigning a circuit element to a distinct process is impossible. The values obtained from different temperatures at a constant RH = 98% can be used to determine activations energies E_A of the thermal activated proton migration i.e. ionic conductivity (Equation S2):

$$\ln(\sigma T) = -\frac{E_A}{R} \cdot \frac{1000}{T} + \ln(\sigma_0) \qquad [S2]$$

, where σ is the bulk proton conductivity [S/cm], T is the temperature [K], σ_0 is the pre-factor of the exponential power law, E_A activation energy of proton migration [kJ/mole] and R is the ideal gas constant R = 8.314 J/mol K.

DVS measurements

The Dynamic Vapor sorption (DVS) measurements were performed using a DVS resolution Dual Vapor Gravimetric Sorption Analyzer (Surface Measurement Systems) at T = 25°C from RH =0 – 95 % with steps of 5%. The solid dry powders were pre-heated in the instrument before the measurement at T = 65°C with RH = 0% for t = 12 h to remove all adsorbed water.

Supplementary Data Analysis 1: Description of TGA/DSC data

The dry crystalline M-struvite powders were analyzed in TGA/DSC from 25-850 °C with 10°C/min to track the evaporation accompanied by the phase transformation during the thermal treatment (Figure S4) and H_2O while the exothermic peak correlates with the crystallization process of M-pyrophosphate. As the mass loss indicates, all struvite compounds release nearly five water molecules and lower amounts of NH_3 per structural formula in the first endothermic peak (Figure S4B). The second endothermic peak at around 150°C in Co-struvite points out to the phase transition of COD mainly to stable NH_4CoPO_4 and $HCoPO_4 \cdot H_2O$ with associated degassing of NH_3 and H_2O (see the theoretical mass loss of 6 H_2O at 38.6 % and 5 H_2O + NH_3 38.3% in Figure S4B). At temperatures ≥ 300°C, these compounds transform further to $HCoPO_4$. The last degassing of the remaining 0.5 H_2O leading to the condensation of M-pyrophosphates proceeds continuously over a broad T interval of 300°C to the crystallization temperature of Co-pyrophosphate at T = 620°C. Although Co-struvite seems to decompose earlier than Ni-struvite (onset temperature at 73°C), it is also the first which crystallizes.

Ni-struvite evaporates mainly water around 90-130°C and forms remanent amorphous phases in dry conditions. These amorphous phases progressively release their volatiles at higher temperatures, resulting in a smooth continuous DSC curve without sharp endothermic signals. Here, the chemical composition ranges most likely from $NH_4NiPO_4 \cdot H_2O$ at 90°C to $HNiPO_4$ < 770°C. $Ni_2P_2O_7$ crystallizes at 770 °C with a sharp exothermic peak. In all samples, the mass change from the crystallization to M-pyrophosphate is not visible in the TGA curve.

In general, the crystallization to $Co_2P_2O_7$ in the TGA/DSC samples happened at significantly higher temperatures than in the isothermally heated samples. Due to the crystallisation kinetics, the heat ramp with 10°C min^{-1} is too fast to track minor proportions of formed $Co_2P_2O_7$ in the TGA or DSC signal. The heating rate and time can significantly influence the absolute phase transition temperature (Figure S4C). This finding indicates the strongly kinetically controlled nature of phase transitions.

The following reaction mass balance equations (Equation S3-S7) are likely to describe the samples' evolution and may be applicable both sequentially or coincidently, resulting in a complex phase composition.

$$NH_4MPO_4 \cdot 6H_2O_{(s)} \rightarrow NH_4MPO_4 \cdot H_2O_{(s)} + 5H_2O_{(g)} \quad [S3]$$

$$NH_4MPO_4 \cdot H_2O_{(s)} \rightarrow NH_4MPO_{4\,(s)} + H_2O_{(g)} \quad [S4]$$

$$NH_4MPO_4 \cdot H_2O_{(s)} \rightarrow HMPO_4 \cdot H_2O_{\,(s)} + NH_{3(g)} \quad [S5]$$

$$NH_4MPO_{4\,(s)} \rightarrow HMPO_{4\,(s)} + NH_{3(g)} \quad [S6]$$

$$2MHPO_{4\,(s)} \rightarrow M_2P_2O_{7\,(s)} + 0.5\ H_2O_{(g)} \quad [S7]$$

Equations S3, S4, S5, S6, S7: Possible reaction equations through the thermal history of the transition metal phosphate compounds.

Supplementary Data Analysis 2: Analysis of the FT-IR/FT-RS spectra

Crystalline precursor M-struvites exhibit IR active vibrations starting with the bending and stretching vibrations of the PO_4^{3-} tetrahedron in the range of 800-550 cm^{-1} for δ(O-P-O) and 1200-850 cm^{-1} for ν(O-P-O) (**Error! Reference source not found.**A, C). These signals are followed by two discrete bands at 1434 cm^{-1} and 1464 cm^{-1} of the stretching mode of NH_4^+ ν(H-N-H). Integration of these bands allows for a semi-quantitative comparison of the amount of bound ammonia in the sample series where the crystalline M-struvite is a reference with one mole NH_4 per sum formula. The calculated amounts are included in the SI (SI: Table S1 and S2). Afterwards, the deformational bending modes of water δ(H-O-H) and ammonia δ(H-N-H) overlap in the range of 1710-1520 cm^{-1}. In the final range of 3800-2200 $cm^{-1,}$ multiple water and ammonia stretching modes appear at coinciding positions. An increase in temperature leads to the continuous depletion of water and ammonia, resulting in the extinction of their IR bands. In all samples, the stretching phosphate bands shift towards higher wavenumbers with increasing temperatures up to 500°C. Above these temperatures, these bands remain at the same positions.

Looking at the phosphate δ- and ν(O-P-O) bands of the Co samples, firstly, the two stretching modes at 874 and 969 cm^{-1} in Co-struvite split into four broad stretching bands of Co-dittmarite at 911, 1018, 1069 and 1102 cm^{-1} while the bending mode shifts from 700 cm^{-1} in Co-struvite to 766 cm^{-1} in Co-dittmarite. When Co-dittmarite decomposes at 180°C, the two sharp δ(H-N-H) peaks form one broader peak with lower intensity at 1420 cm^{-1} while at the same time, the ν(H-O-H) at 3388 cm^{-1} peak extinguishes. In addition, multiple phosphate bands in the range of 1150 – 850 cm^{-1} appear due to possibly several phosphate phases. With progressively increasing temperatures these stretching modes of the phosphate bonding rearrange to two broad peaks at 1000 cm^{-1} and 909 cm^{-1} at 300°C indicative for higher degree of condensation of the phosphate units in NH_4CoPO_4.

The Raman spectra correlate mainly with the IR bands (**Error! Reference source not found.**B, D). Generally, at around 3200-2800 $cm^{-1,}$ stretching vibrations of water and ammonia $\nu(H_2O)$, $\nu(NH_3)$ appear in the samples. At around 1600 and 1400 $cm^{-1,}$ distinct bending modes of ammonia are observed. In the Ni- and Co systems, from roughly 1250-1050 $cm^{-1,}$ symmetric and asymmetric stretching bands belonging to the phosphate tetrahedron $\nu_s(PO_4)$, and $\nu_{as}(PO_4)$ represent the most significant bands. All stretching $\nu(PO_4)$ modes show a progressive shift towards higher wavenumbers with increasing temperature (dotted arrow in **Error! Reference source not found.**). Finally, at 750-600 $cm^{-1,}$ first, the stretching vibrations of the P-O-P bridges, and secondly, at 600-400 cm^{-1} the bending vibrations of the phosphate unit $\delta(PO_4)$ and δ(P-O-P) show up. The general order of modes was observed to be $\nu_{as}(PO_4) > \nu_s(PO_4) > \nu_{as}$(P-O-P) > ν_s(P-O-P) > $\delta(PO_4)$ > δ(P-O-P) in agreement with other phosphate phases reported in the literature[4, 5]. As the temperature increases, the asymmetric stretching vibrations vas(PO4) and ν(P-O-P) increase in both metal systems, indicating a progressive transformation of ortho- to pyrophosphate. Since multiple crystalline phase transitions are involved in the Co-system in the thermal history, the shift of the phosphate modes is not as significant in the Ni-system, which includes mostly the amorphous phase. Amorphous phases form wide Raman bands of low intensity compared to crystalline phases with narrower, more intense bands. Therefore, the trend in the extent of crystallinity is reflected in the changing width of the Raman bands of the samples.

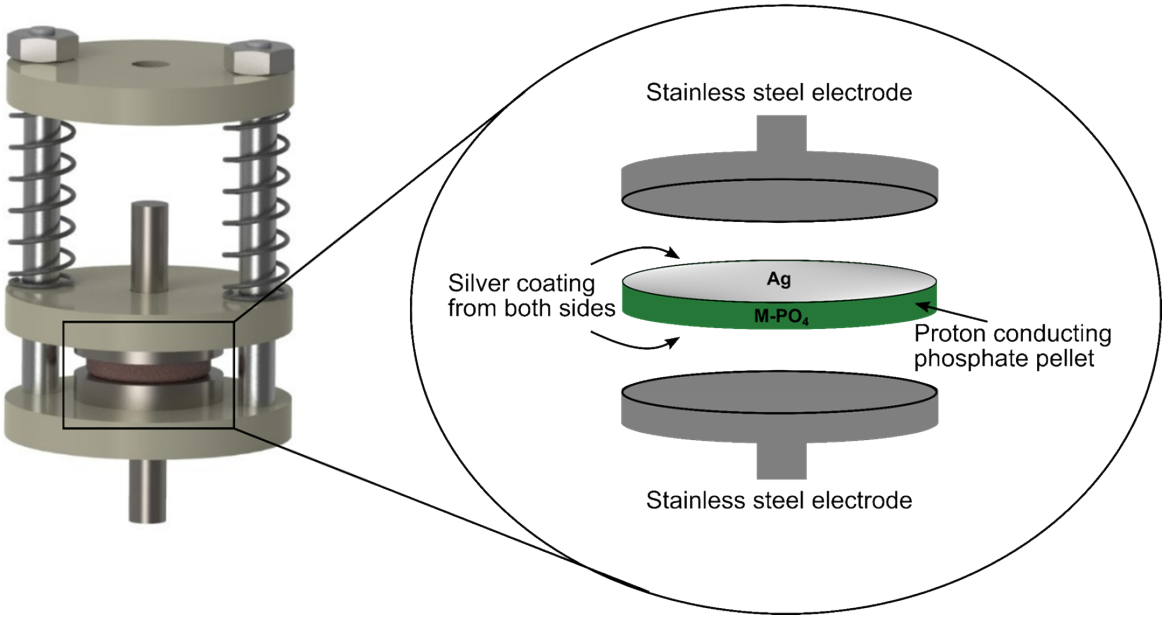

Figure S1: The proton conductivity measurement setup with an overview on the left and an exploded view on the right; The compressed pellet is clamped by two mechanical springs; the conductive metal parts of the spring and bars do not touch the electrode setup to avoid any interference in measuring of the current/voltage.

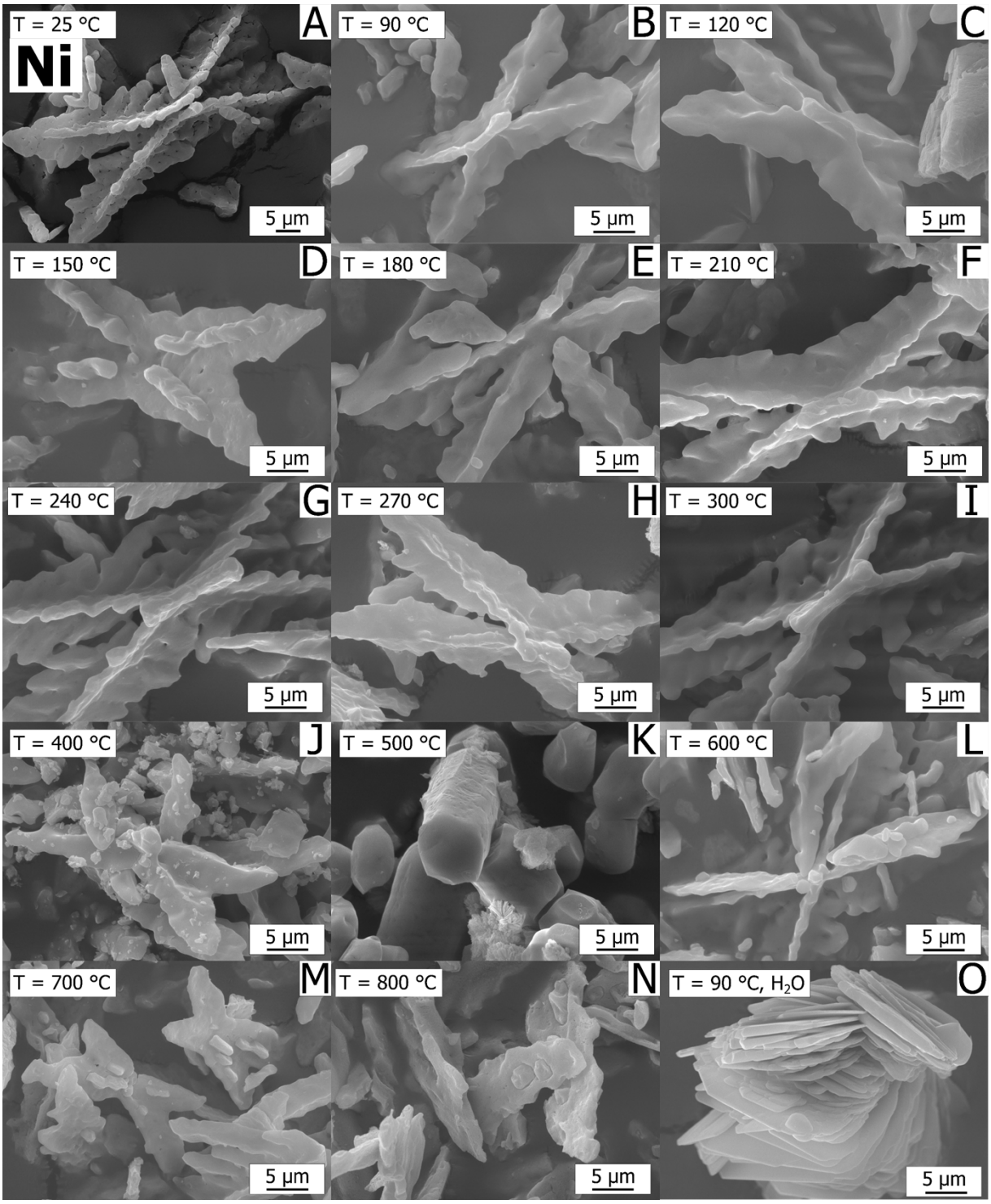

Figure S2: SE images of full T-series of a thermally treated Ni-struvite; (A) precursor Ni-struvite at 25°C; thermally Ni-struvite thermally treated at (B) 90°C; (C)120°C; (D) 150°C ; (E) 180°C; (F) 210°C; (G) 240°C; (H) 270°C; (I) 300°C; (J) 400°C ; (K) 500°C; (L) 600°C; (M) 700°C; (N) 800°C; (O) Ni-struvite hydrothermally treated at T = 90°C and at RH ~ 100%.

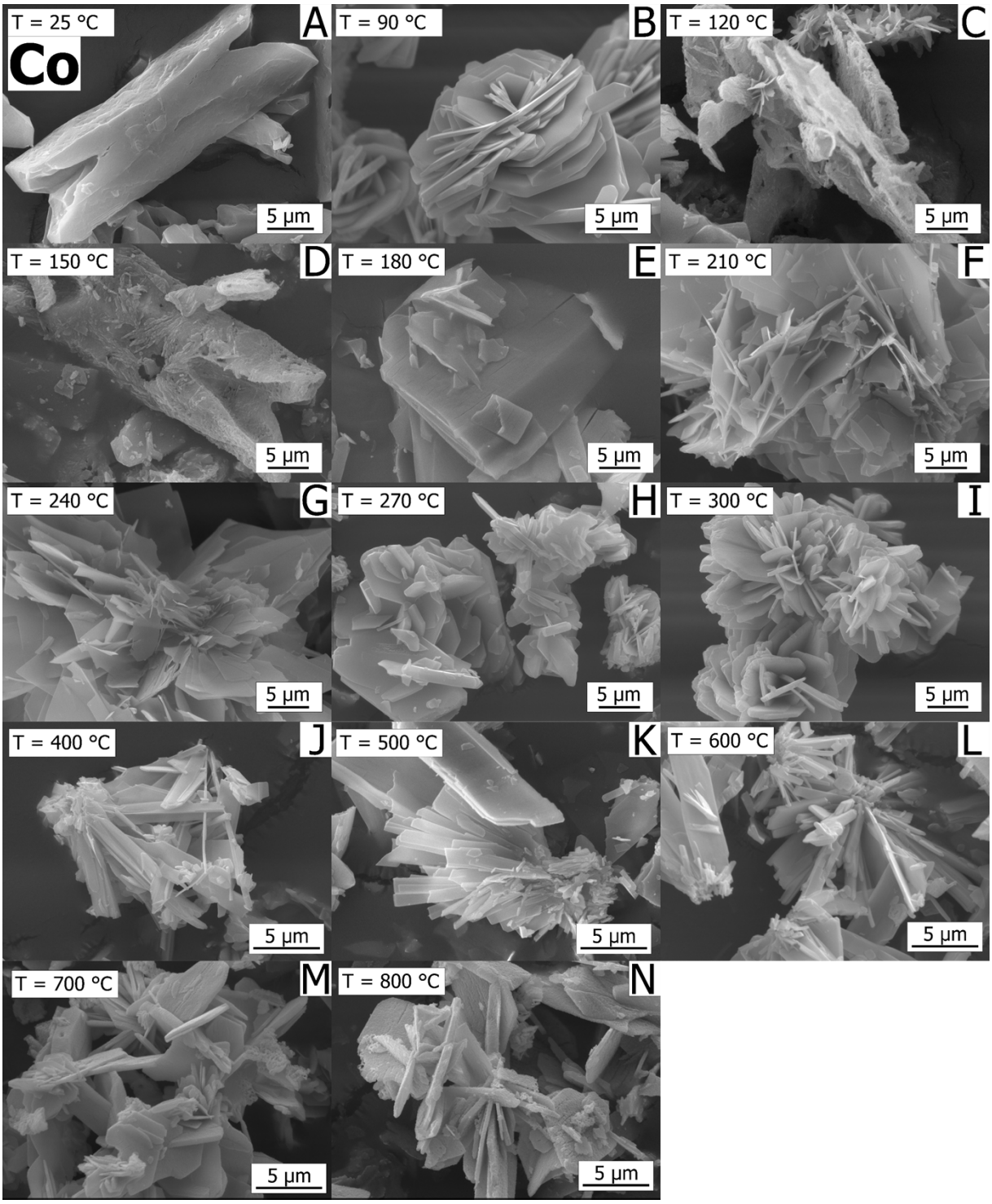

Figure S3: SE images of full T-series of a thermally treated Co-struvite; (A) precursor Co-struvite at 25°C; Co-struvite thermally treated at (B) 90°C; (C) 120°C ; (D) 150°C ; (E) 180°C; (F)210°C; (G)240°C; (H)270°C; (I) 300°C; (J) 400°C ; (K) 500°C; (L) 600°C; (M) 700°C; (N) 800°C.

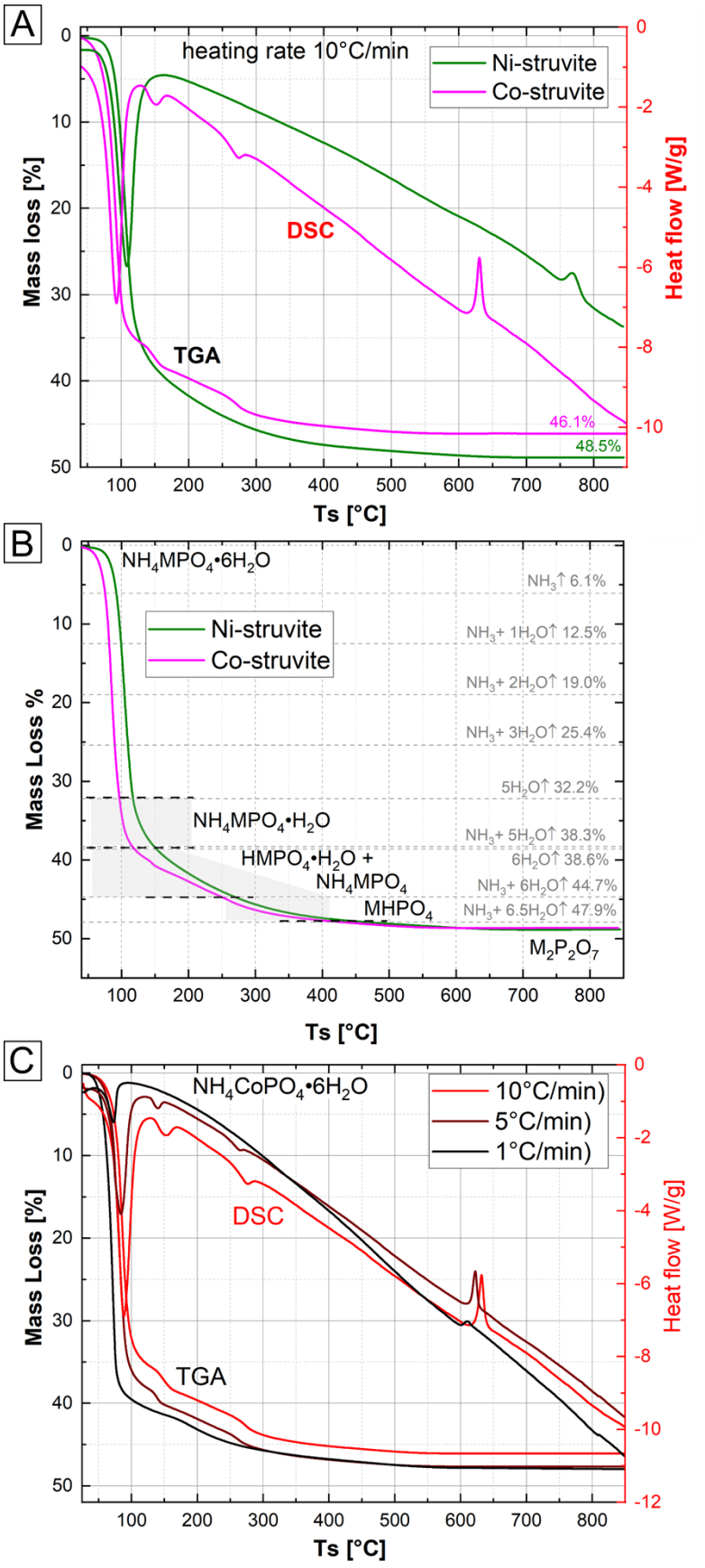

Figure S4: (A) TGA/DSC profiles for the pure M-struvite (M = Ni and Co) with labels indicating the final mass loss; (B) TGA graphs for the pure M-struvite (M = Ni and Co) with the labels indicating theoretical calculated mass loss and associated theoretical phase compositions. (C) TGA/DSC curves of Co-struvite with varying heating rates (1°C, 5°C and 10°C/min) show changes in the occurrence of the thermal events.

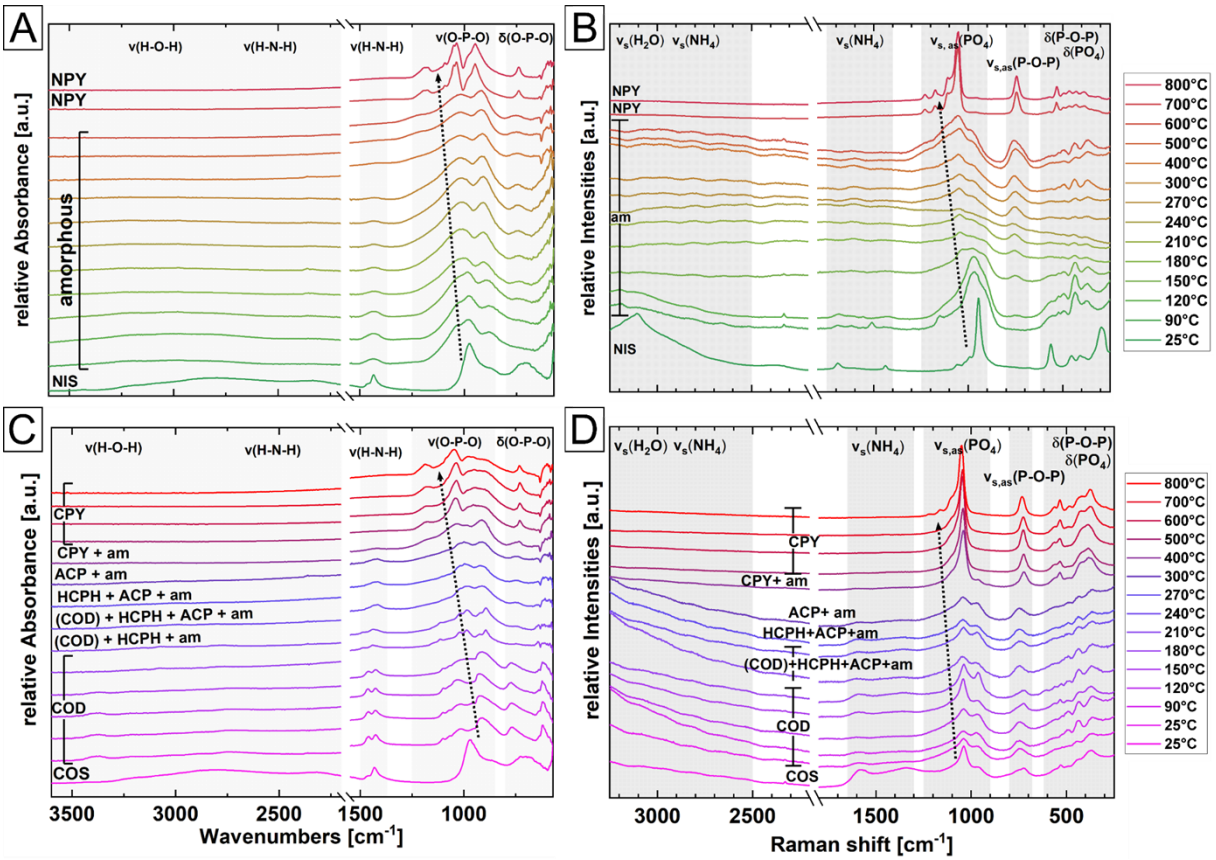

Figure S5: (A) Fourier transformed-infrared (FT-IR) and (B) Raman spectra (FT-RS) of Ni T-series (green-red) and (C) FT-IR + (D) Raman spectra of Co T-series (pink-red) in the range of 25°C ≤ T ≤ 800°C; The distinct stretching (ν) and bending (δ), symmetric (s) or asymmetric (as) modes of the phosphate, water, and ammonium units are displayed and marked in grey; The degree of pyrophosphatisation is marked by the dotted arrow; Raman spectra: All peaks were normalised against the intensity of the $\nu_s(PO_4)$ mode (relative Intensities [a.u.]); the corresponding XRD-derived phase compositions at given temperature were added to the respective spectra.

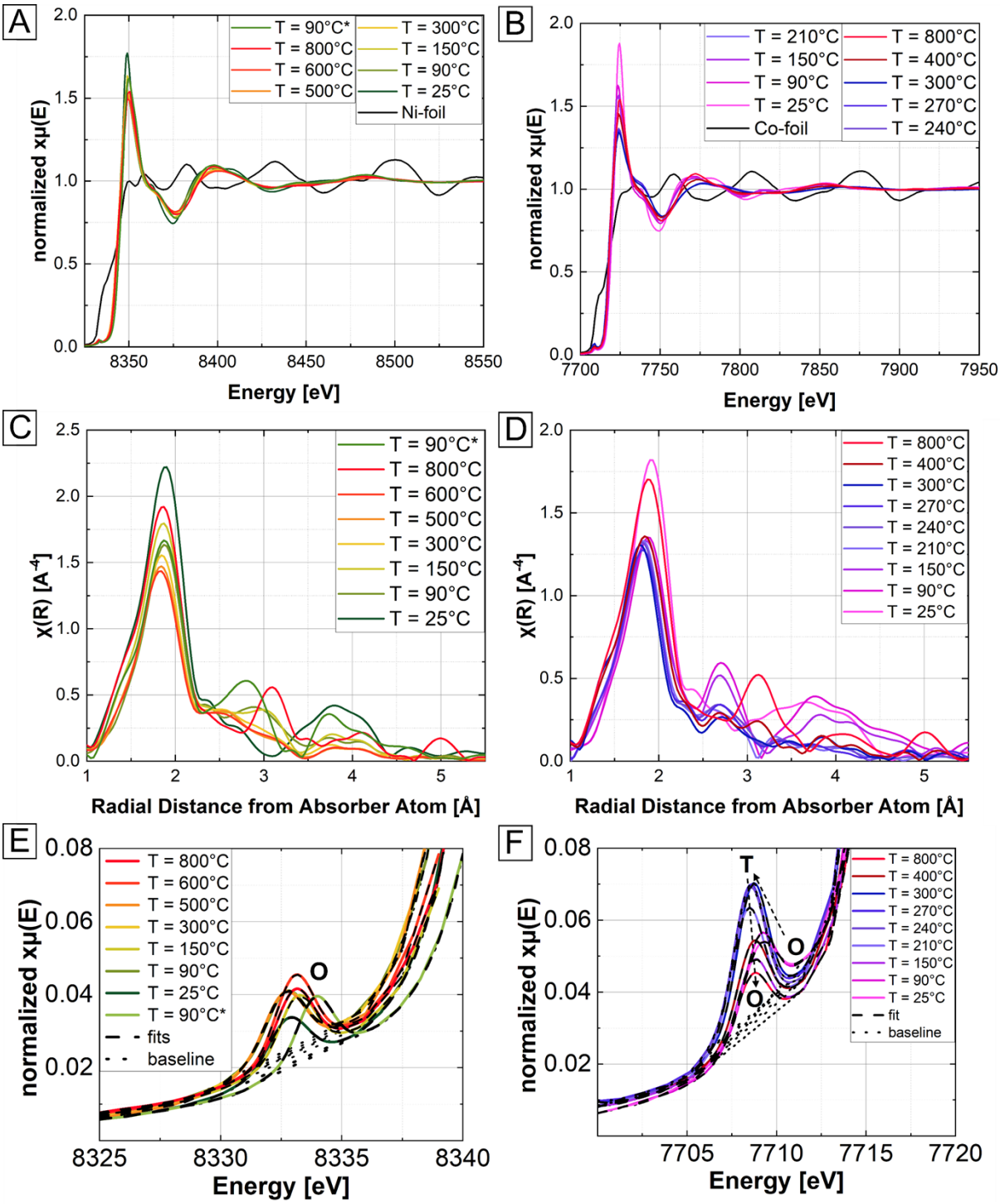

Figure S6: XAS spectra of all thermally processed TMPs plotted in the real space (A,B) and in the R-space (C,D) 90°C* = hydrothermal synthesis at RH ≈ 100% at 90°C. (E, F) Pre-peak region of Ni- and Co-phosphate and the integration from Gaussian fits, O = Octahedron, T = Tetrahedron.

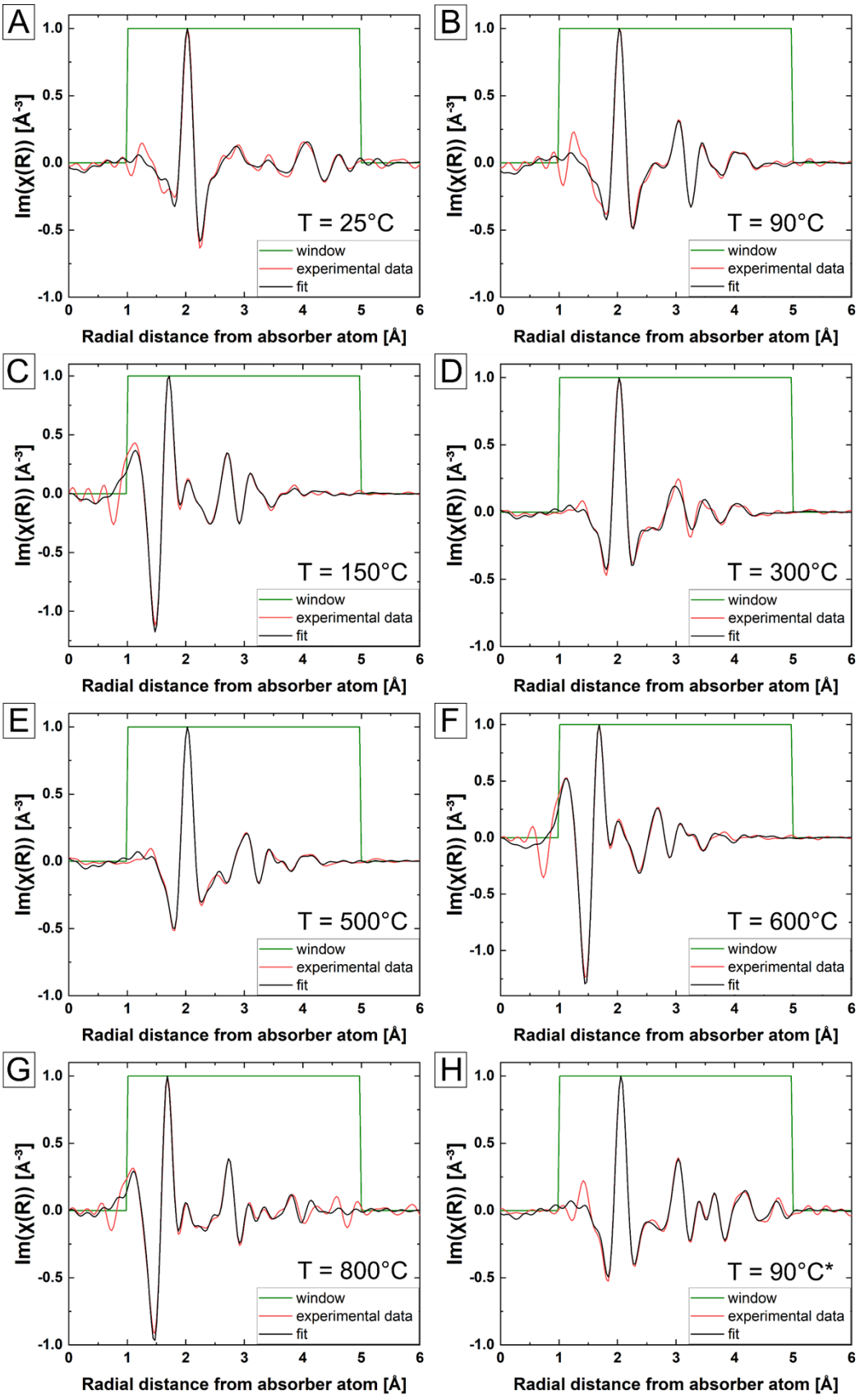

Figure S7: Fits: Ni- K-edge EXAFS data shown in real space for (A) Ni-struvite, T = 25°C, R = 0.011; (B) amorphous phase heated at 90°C, R = 0.008; (C) amorphous phase heated at 150°C, R = 0.003; (D) amorphous phase heated at 300°C, R = 0.004; (E) amorphous phase heated at 500°C, R = 0.003; (F) amorphous phase heated at 600°C, R = 0.003; (G) $Ni_2P_2O_7$ heated at 800°C, R = 0.011; (H) Ni-dittmarite heated hydrothermally at 90°C , R = 0.008.

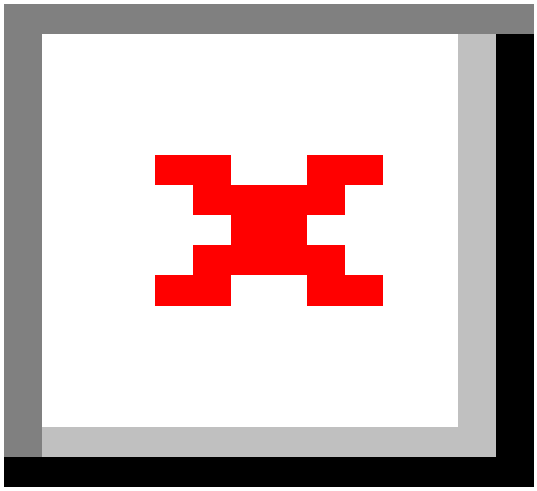

Figure S8: Fits of Co- K-edge EXAFS data shown in real space for (A) Co-struvite at 25°C, R = 0.014; (B) Co-dittmarite at 90°C, R = 0.007; (C) Co-dittmarite at 150°C, R = 0.011; (D) HCPH , ACP, amorphous phase and Co-dittmarite at 210°C, R = 0.007; (E) ACP, HCPH and amorphous phase at 240°C, R = 0.011; (F) ACP, HCPH and amorphous phase at 270°C, R = 0.007; (G) ACP and amorphous phase at 300°C, R = 0.010; (H) $Co_2P_2O_7$ and amorphous phase at 400°C, R = 0.005; (I) $Co_2P_2O_7$ at 800°C, R = 0.015

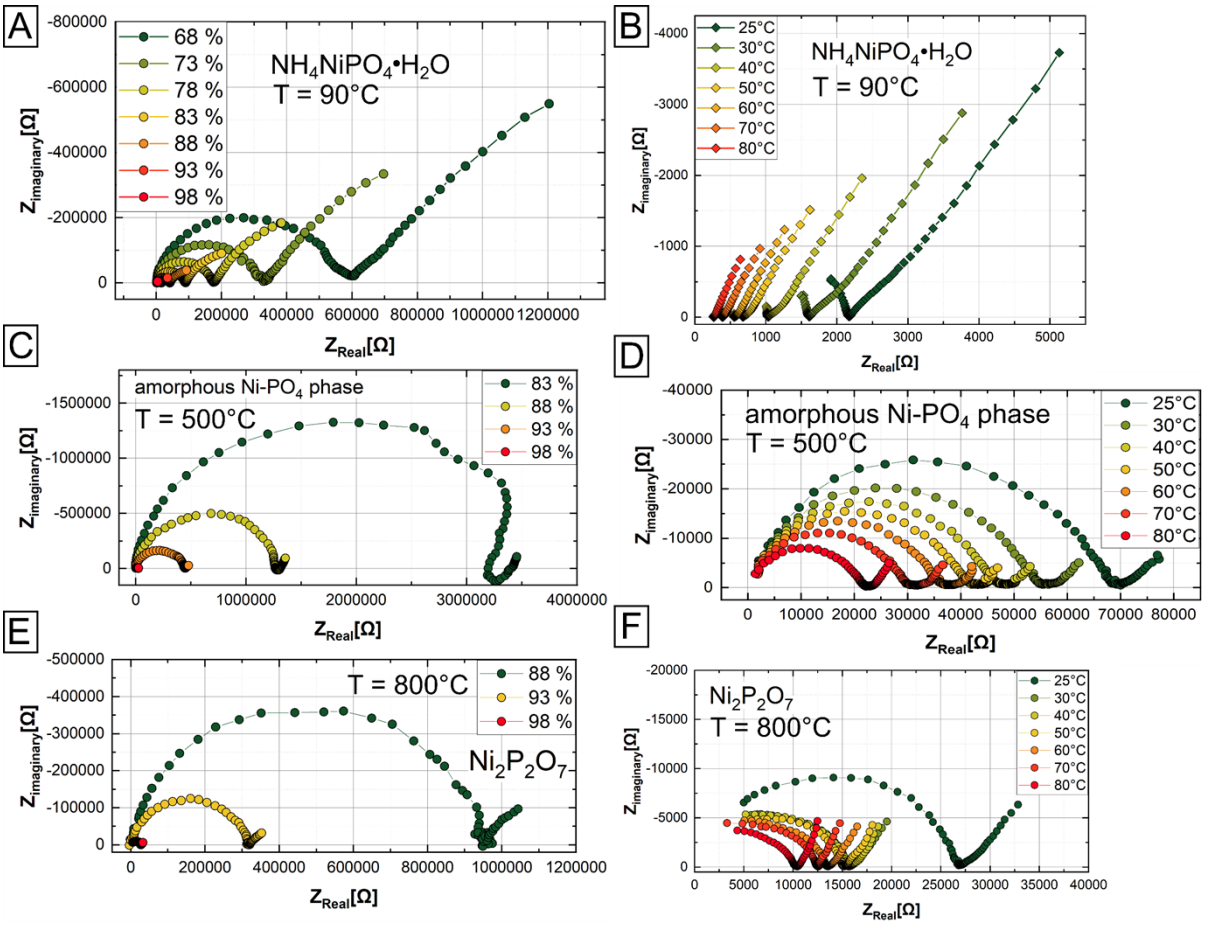

Figure S9: Nyquist plots of PC data at relative humidity values RH = 68%-98% at a constant temperature T = 25°C, and at different temperatures 25°C – 90°C at constant RH of 98%; Nyquist plots show real and imaginary impedance on x- and y-axis, respectively. Nyquist plots of Ni-dittmarite $NH_4NiPO_4 \cdot H_2O$ $Pmn2_1$ heated at T = 90°C (A) at various RH and (B) at various temperatures; Nyquist plots of amorphous Ni-PO_4 phase heated at T = 500°C (D) at various RH and (E) at various temperatures; Nyquist plots of NPY heated at T = 800°C (E) at various RH and (F) at various temperatures.

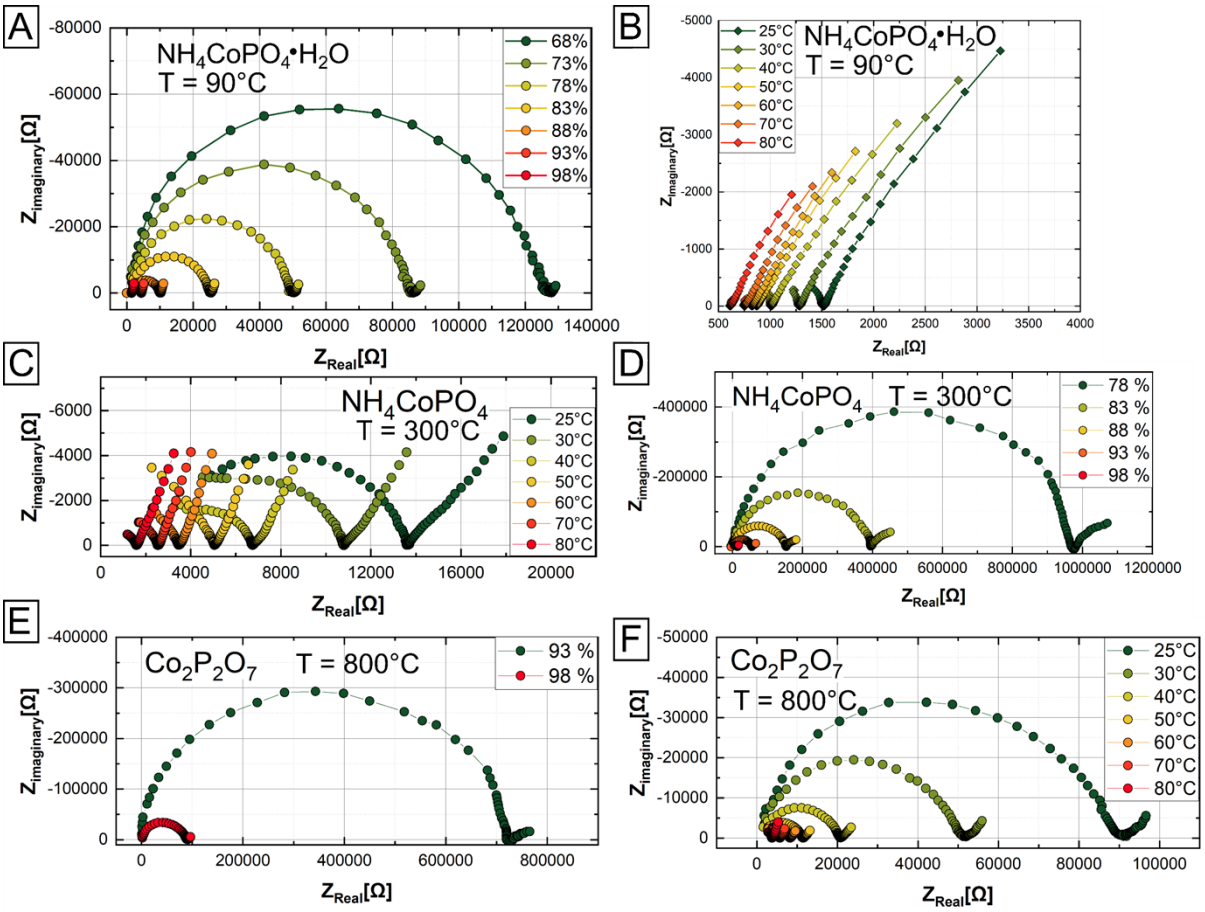

Figure S10: Nyquist plots of PC data at different relative humidities RH = 68%-98% with a constant temperature T = 25°C, at different temperatures 25°C – 90°C with a constant RH of 98 % Nyquist plots of Co-dittmarite $NH_4CoPO_4{\cdot}H_2O$ $Pmn2_1$ heated at T = 90°C (A) at various RH and (B) at various temperatures; Nyquist plots of ACP, NH_4CoPO_4 heated at T = 300°C (C) at various RH and (D) at various temperatures; Nyquist plots of CPY heated at T = 800°C (E) at various RH and (F) at various temperatures.

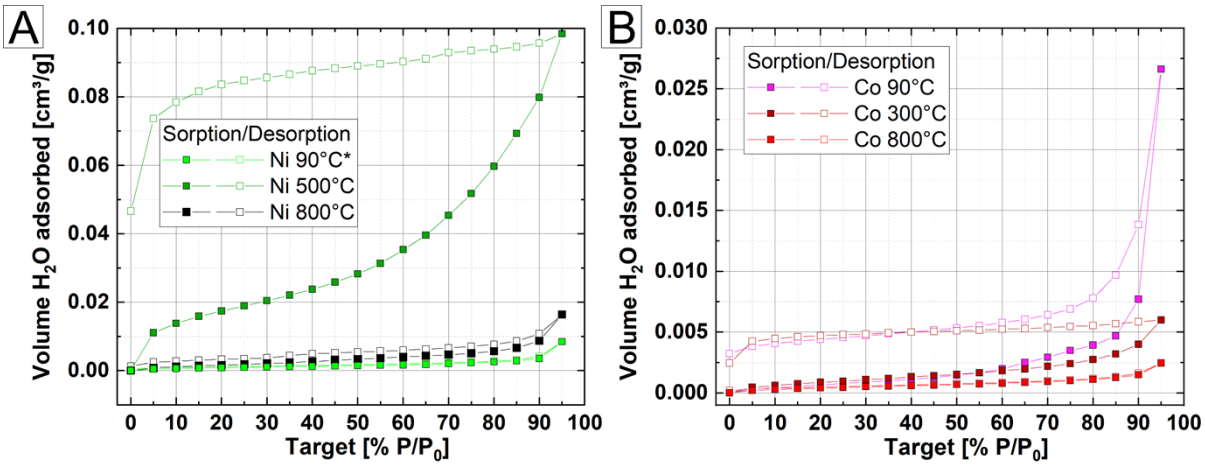

Figure S11: DVS isotherms of (A) Ni- and (B) Co-phosphate compounds; Ni 90°C* = hydrothermal synthesized at T = 90°C and nearly 100% RH.

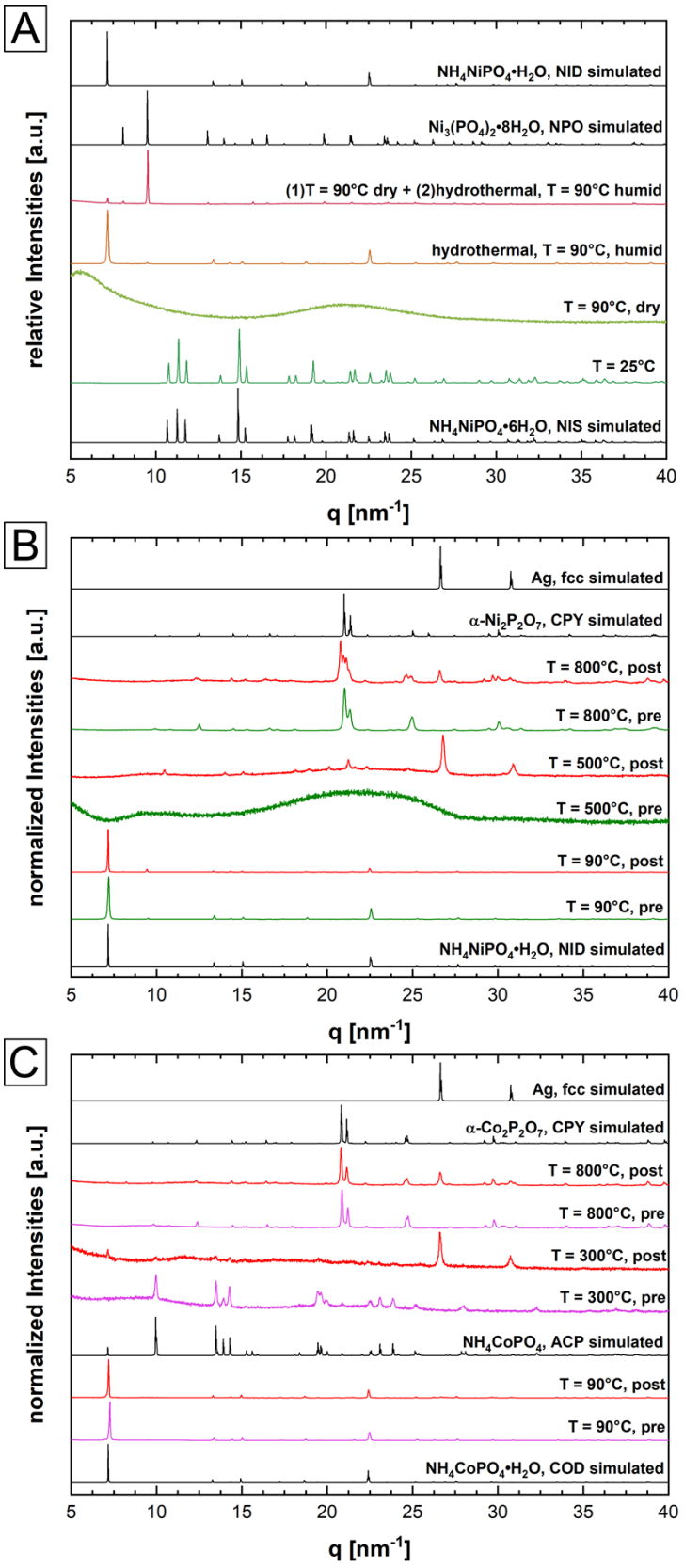

Figure S12: XRD patterns of (A) Ni-struvite thermal processed in different conditions, (B) of Nickel phosphate phases and (C) Cobalt phosphate phases before and after the proton conductivity measurement; Ni-struvite (NIS) reference database ICSD 403058; Ni-dittmarite (NID) reference database ICSD 424553; Ni-phosphate octahydrate (NPO) reference database ICSD 240946; α-$Ni_2P_2O_7$ (NPY) reference ICSD 403058; Co-dittmarite (COD) with COD reference database 2008122; α-NH_4CoPO_4 (ACP) reference PDF 00-018-0402; α-$Co_2P_2O_7$ (CPY) reference database ICSD 280959; Ag (fcc) COD reference database 9013045.

Table S1: Calculated amount of ammonia normalized on the Ni-struvite from the FT-IR spectra of the Ni-samples with their respective phase composition based on the integration of the modes of H-N-H at 1464 cm^{-1} and 1434 cm^{-1} (NIS = Ni-Struvite $NH_4NiPO_4 \cdot 6H_2O$, NPY = Nickelpyrophosphate $Ni_2P_2O_7$, am = amorphous phase, N.P. = not present).

phase composition	T[°C]	NH_4 content (FT-IR)
Ni-struvite	25	100
am	90	67
am	120	78
am	150	71
am	180	36
am	210	35
am	240	31
am	270	26
am	300	24
am	400	9
am	500	N.P.
am	600	N.P.
NPY	700	N.P.
NPY	800	N.P.

Table S2: Calculated amount of ammonia normalized on the Co-struvite from the FT-IR spectra of the Co-samples with their respective phase composition based on the integration of the modes of H-N-H at 1464 cm^{-1} and 1434 cm^{-1} (COS = Co-struvite $NH_4CoPO_4 \cdot 6H_2O$, COD = Co-dittmarite $NH_4CoPO_4 \cdot H_2O$, HCPH = hydrogencobalt(II)phosphate hydrate $HCoPO_4 \cdot H_2O$, ACP = ammoniumcobalt(II)phosphate NH_4CoPO_4, CPY = cobaltpyrophosphate $Co_2P_2O_7$, am = amorphous phase, N.P. = not present).

phase composition	T[°C]	NH_4 content (FT-IR)
COS	25	100
COD	25	100
COD	90	71
COD	120	68
COD	150	60
COD	180	40
HCPH+ACP+am+(COD)	210	39
HCPH+ACP+am	240	39
HCPH+ACP+am	270	32
ACP + am	300	31
CPY + am	400	8
CPY + am	500	N.P.
CPY	600	N.P.
CPY	700	N.P.
CPY	800	N.P.

Table S3: Calculated integration results [R^2, integrated area App, Full Width Half Maximum (FWHM), centre of the peak and maximum height] from the pre-peak region of the thermal treated Ni- and Co-Phosphate samples with their respective phase composition; The distinct peak was fitted by a Gaussian model and then integrated over this region; The calculated pre-peak area values A_{pp} represent more semi-quantitative and are of a comparative purpose rather than show absolute values.

Prepeak area integration results					fit function: Gaussian		
T [°C]	**Sample**	chemical formula	R^2 value	Pre-peak Area A_{pp} (err)	FWHM	Center	Max. Height
25	Co-struvite	$NH_4CoPO_4{\cdot}6H_2O$	0.990	0.026(1)	2.15	7709.0	0.011
90	Co-dittmarite	$NH_4CoPO_4{\cdot}H_2O$	0.991	0.032(1)	1.99	7709.0	0.015
150	Co-dittmarite	$NH_4CoPO_4{\cdot}6H_2O$	0.990	0.041(2)	1.99	7708.7	0.019
210	HCPH, ACP, am, (COD)	NH4CoPO4, HCoPO4·H2O, NH4CoPO4·H2O, am	0.996	0.071(1)	2.08	7708.0	0.032
240	HCPH, ACP, am	NH4CoPO4, HCoPO4·H2O, am	0.991	0.077(3)	2.02	7708.5	0.036
270	HCPH, ACP, am	NH4CoPO4, HCoPO4·H2O, am	0.992	0.078(3)	2.03	7708.5	0.036
300	ACP, am	NH4CoPO4, am	0.994	0.075(3)	2.03	7708.0	0.035
400	CPY, am	Co2P2O7, am	0.994	0.048(1)	1.98	7708.7	0.023
800	CPY	Co2P2O7	0.995	0.033(1)	1.99	7708.7	0.016
25	Ni-struvite	$NH_4NiPO_4{\cdot}6H_2O$	0.992	0.028(2)	1.97	8333.3	0.013
90	am	am	0.999	0.032(2)	1.86	8333.0	0.016
150	am	am	0.999	0.030(1)	1.71	8333.2	0.016
300	am	am	0.985	0.034(2)	1.95	8333.0	0.016
500	am	am	0.993	0.036(1)	1.97	8333.0	0.017
600	am	am	0.999	0.041(2)	1.83	8333.1	0.021
800	NPY	$Ni_2P_2O_7$	0.998	0.033(1)	1.78	8333.1	0.017
90, 100% H_2O	Ni-dittmarite	$NH_4NiPO_4{\cdot}H_2O$	0.999	0.029(2)	1.69	8333.9	0.016

Table S4: Fit parameter for Ni-struvite at room temperature T = 25°C, R-factor= 0.011.

sample	scattering path	N	σ^2	R_{diff} [Å]	R_{diff}^2 [Å^2]	R_{model} [Å]	R_{fit} [Å]
Ni-struvite (25°C)	Ni1-O1	**6.7(7)**	0.008	3.00E-04	9.00E-08	2.046	2.046
$NH_4NiPO_4 \cdot 6H_2O$	Ni1-H1	2	0.046	6.31E-02	3.98E-03	2.365	2.428
R-factor	Ni1-H2	5	0.046	6.31E-02	3.98E-03	2.586	2.649
0.011	Ni1-H3	2	0.046	6.31E-02	3.98E-03	2.627	2.690
S_O^2 (err)	Ni1-H4	2	0.046	6.31E-02	3.98E-03	2.668	2.731
1.7(4)	Ni1-N1	1	0.023	-6.53E-01	4.26E-01	4.022	3.369
ΔE (err)	Ni1-N2	2	0.023	-6.53E-01	4.26E-01	4.111	3.458
2.6(7)	Ni1-O2	4	0.005	2.87E-01	8.24E-02	4.084	4.371
S_O^2 O1 (set)	Ni1-O3	2	0.005	2.87E-01	8.24E-02	4.200	4.487
1.0	Ni1-O4	3	0.005	2.87E-01	8.24E-02	4.272	4.559
	Ni1-O5	2	0.005	2.87E-01	8.24E-02	4.329	4.616
	Ni1-P1	2	0.005	2.87E-01	8.24E-02	4.368	4.655
	Ni1-O6	2	0.005	2.87E-01	8.24E-02	4.820	5.107

Table S5: Fit parameter for amorphous Ni-PO_4 phase heated at T = 90°C, R-factor= 0.008.

sample	scattering path	N	σ^2	R_{diff} [Å]	R_{diff}^2 [Å^2]	R_{model} [Å]	R_{fit} [Å]
Ni 90°C, am	Ni1-O1	**5.5(4)**	0.008	5.24E-02	2.75E-03	2.089	2.037
	Ni1-O2	2	0.009	2.15E-01	4.61E-02	3.283	3.069
R-factor	Ni1-P1	2	0.041	3.43E-02	1.18E-03	3.187	3.152
0.008	Ni1-P2	1	0.041	3.43E-02	1.18E-03	3.274	3.240
S_O^2 (err)	Ni1-O3	2	0.009	2.15E-01	4.61E-02	3.546	3.331
2.7(8)	Ni1-Ni2	4	0.019	2.21E-01	4.87E-02	3.673	3.452
ΔE (err)	Ni1-O4	2	0.009	2.15E-01	4.61E-02	3.767	3.552
-0.7(8)	Ni1-O5	2	0.009	2.15E-01	4.61E-02	3.800	3.585
S_O^2 O1 (set)	Ni1-O6	1	0.027	-3.91E-01	1.53E-01	3.878	4.269
1.0	Ni1-O7	2	0.027	-3.91E-01	1.53E-01	4.111	4.502
	Ni1-O8	2	0.027	-3.91E-01	1.53E-01	4.160	4.551
	Ni1-O9	2	0.027	-3.91E-01	1.53E-01	4.224	4.615
	Ni1-O10	1	0.027	-3.91E-01	1.53E-01	4.498	4.889
	Ni1-O11	2	0.027	-3.91E-01	1.53E-01	4.733	5.124

Table S6: Fit parameter for amorphous Ni-PO_4 phase heated at T = 150°C, R-factor= 0.003.

sample	scattering path	N	σ^2	R_{diff} [Å]	R_{diff}^2 [Å^2]	R_{model} [Å]	R_{fit} [Å]
Ni 150°C, am	Ni1-O1	**6.3(4)**	0.009	9.44E-03	8.91E-05	2.046	2.055
	Ni1-P1	1	0.013	9.26E-02	8.58E-03	2.734	2.827
R-factor	Ni1-P2	2	0.013	9.26E-02	8.58E-03	3.187	3.279
0.003	Ni1-P3	1	0.013	9.26E-02	8.58E-03	3.274	3.367
S_O^2 (err)	Ni1-O2	2	0.002	9.49E-02	9.00E-03	3.283	3.378
1.0(4)	Ni1-Ni2	4	0.026	-1.62E-01	2.62E-02	3.673	3.511
ΔE (err)	Ni1-O3	4	0.010	2.57E-02	6.61E-04	3.546	3.571
3.6(9)	Ni1-O4	2	0.026	-1.62E-01	2.62E-02	3.767	3.605
S_O^2 O1 (set)	Ni1-O5	1	0.026	-1.62E-01	2.62E-02	3.878	3.717
0.91	Ni1-O6	2	0.010	2.57E-02	6.61E-04	3.800	3.826
	Ni1-O7	2	0.026	-1.62E-01	2.62E-02	4.111	3.949
	Ni1-O8	2	0.026	-1.62E-01	2.62E-02	4.160	3.998
	Ni1-O9	2	0.026	-1.62E-01	2.62E-02	4.224	4.063
	Ni1-O10	1	0.026	-1.62E-01	2.62E-02	4.498	4.336
	Ni1-O11	2	0.026	-1.62E-01	2.62E-02	4.690	4.528
	Ni1-O12	2	0.026	-1.62E-01	2.62E-02	4.733	4.572
	Ni1-Ni3	2	0.026	-1.62E-01	2.62E-02	4.747	4.585

Table S7: Fit parameter for amorphous Ni-PO_4 phase heated at T = 300°C, R-factor= 0.004.

sample	scattering path	N	σ^2	R_{diff} [Å]	R_{diff}^2 [Å^2]	R_{model} [Å]	R_{fit} [Å]
Ni 300°C, am	Ni1-O1	**5.5(4)**	0.008	3.60E-03	1.30E-05	2.043	2.040
	Ni1-P1	1	0.009	-3.76E-02	1.42E-03	2.734	2.772
R-factor	Ni1-P2	2	0.041	-3.76E-02	1.42E-03	3.187	3.224
0.004	Ni1-P3	1	0.041	-3.76E-02	1.42E-03	3.274	3.312
S_O^2 (err)	Ni1-Ni2	4	0.009	2.19E-01	4.79E-02	3.673	3.454
3(2)	Ni1-O2	2	0.019	-2.27E-01	5.13E-02	3.283	3.510
ΔE (err)	Ni1-O3	2	0.009	-2.27E-01	5.13E-02	3.546	3.772
-0.3(4)	Ni1-N1	1	0.009	2.19E-01	4.79E-02	4.028	3.810
S_O^2 O1 (set)	Ni1-O4	2	0.027	-2.27E-01	5.13E-02	3.767	3.993
0.87	Ni1-O5	2	0.027	-2.27E-01	5.13E-02	3.800	4.027
	Ni1-O6	2	0.027	-1.42E-01	2.01E-02	4.111	4.253
	Ni1-O7	2	0.027	-1.42E-01	2.01E-02	4.160	4.302
	Ni1-O8	2	0.027	-2.27E-01	5.13E-02	4.224	4.451
	Ni1-O9	1	0.027	-1.42E-01	2.01E-02	4.498	4.640

Table S8: Fit parameter for amorphous Ni-PO4 phase heated at T =500°C, R-factor= 0.003.

sample	scattering path	N	σ^2	R_{diff} [Å]	R_{diff}^2 [Å^2]	R_{model} [Å]	R_{fit} [Å]
Ni 500°C, am	Ni1-O1	**5.3(2)**	0.009	3.38E-02	1.14E-03	2.060	2.026
	Ni1-Ni2	1	0.006	2.26E-01	5.10E-02	3.191	2.966
R-factor	Ni1-P1	1	0.001	1.34E-02	1.81E-04	3.017	3.004
0.003	Ni1-P2	2	0.001	1.34E-02	1.81E-04	3.223	3.210
S_O^2 (err)	Ni1-P3	1	0.001	1.35E-02	1.81E-04	3.371	3.357
-3.2(3)	Ni1-O2	1	0.013	-2.42E-01	5.86E-02	3.311	3.553
ΔE (err)	Ni1-O3	1	0.013	-2.42E-01	5.86E-02	3.423	3.665
0.7(1)	Ni1-O4	1	0.013	-2.42E-01	5.86E-02	3.459	3.701
S_O^2 O1 (set)	Ni1-O5	1	0.013	-2.42E-01	5.86E-02	3.570	3.812
0.87	Ni1-O6	1	0.013	-2.42E-01	5.86E-02	3.640	3.882
	Ni1-O7	1	0.013	-2.42E-01	5.86E-02	3.747	3.989
	Ni1-P4	1	0.007	-2.07E-01	4.26E-02	3.997	4.204
	Ni1-O8	1	0.013	-2.42E-01	5.86E-02	3.985	4.227
	Ni1-O9	4	0.013	-2.42E-01	5.86E-02	4.264	4.507

Table S9: Fit parameter for amorphous Ni-PO4 phase heated at T =600°C, R-factor= 0.003.

Sample	Scattering path	N	σ^2	R_{diff} [Å]	R_{diff}^2 [Å^2]	R_{model} [Å]	R_{fit} [Å]
Ni 600°C am	Ni1-O1	**5.5(2)**	9.57E-03	-5.06E-02	2.56E-03	2.060	2.009
	Ni1-Ni2	1	2.75E-02	-2.23E-01	4.97E-02	3.191	2.969
R-factor	Ni1-O2	1	5.52E-03	-1.07E-02	1.14E-04	3.311	3.300
0.003	Ni1-P1	1	1.75E-02	3.18E-01	1.01E-01	3.017	3.335
S_O^2 (err)	Ni1-O3	1	5.52E-03	-1.07E-02	1.14E-04	3.423	3.412
2.7(4)	Ni1-O4	1	5.52E-03	-1.07E-02	1.14E-04	3.459	3.448
ΔE (err)	Ni1-P2	2	1.75E-02	3.18E-01	1.01E-01	3.223	3.541
-5.6(4)	Ni1-O5	1	5.52E-03	-1.07E-02	1.14E-04	3.570	3.560
S_O^2 O1 (set)	Ni1-O6	1	5.52E-03	-1.07E-02	1.14E-04	3.640	3.629
0.91	Ni1-P3	1	1.75E-02	3.18E-01	1.01E-01	3.371	3.688
	Ni1-O7	1	1.92E-02	6.42E-02	4.13E-03	3.747	3.811
	Ni1-O8	1	1.92E-02	6.42E-02	4.13E-03	3.985	4.049
	Ni1-P4	1	1.75E-02	3.18E-01	1.01E-01	3.997	4.315
	Ni1-O9	4	1.92E-02	6.42E-02	4.13E-03	4.264	4.329

Table S10: Fit parameter for $Ni_2P_2O_7$ heated at T =800°C, R-factor= 0.011.

sample	scattering path	N	σ^2	R_{diff} [Å]	R_{diff}^2 [Å^2]	R_{model} [Å]	R_{fit} [Å]
Ni 800°C	Ni1-O1	**5.6(3)**	7.23E-03	-3.02E-02	9.14E-04	2.060	2.030
$Ni_2P_2O_7$	Ni1-P1	1	5.31E-03	3.51E-02	1.23E-03	3.017	3.052
R-factor	Ni1-Ni2	1	8.40E-03	-1.09E-01	1.19E-02	3.191	3.082
0.011	Ni1-O2	1	8.40E-03	-1.09E-01	1.19E-02	3.311	3.202
S_O^2 (err)	Ni1-P2	2	5.31E-03	3.51E-02	1.23E-03	3.223	3.258
0.9(2)	Ni1-O3	1	2.50E-04	-8.46E-02	7.16E-03	3.423	3.338
ΔE (err)	Ni1-O4	1	2.50E-04	-8.46E-02	7.16E-03	3.459	3.374
-0.8(6)	Ni1-P3	1	5.31E-03	3.51E-02	1.23E-03	3.371	3.406
S_O^2 O1 (set)	Ni1-O5	1	2.50E-04	-8.46E-02	7.16E-03	3.570	3.486
0.91	Ni1-O6	1	2.50E-04	-8.46E-02	7.16E-03	3.640	3.555
	Ni1-O7	1	2.50E-04	-8.46E-02	7.16E-03	3.747	3.662
	Ni1-P4	1	5.31E-03	3.51E-02	1.23E-03	3.997	4.032
	Ni1-O8	1	5.50E-03	7.58E-02	5.74E-03	3.985	4.061
	Ni1-Ni3	1	8.40E-03	-1.09E-01	1.19E-02	4.223	4.114
	Ni1-P5	1	5.31E-03	3.51E-02	1.23E-03	4.275	4.310
	Ni1-O9	4	5.50E-03	7.58E-02	5.74E-03	4.264	4.340
	Ni1-O10	1	5.50E-03	7.58E-02	5.74E-03	4.393	4.468
	Ni1-O11	1	5.50E-03	7.58E-02	5.74E-03	4.450	4.526
	Ni1-O12	2	5.50E-03	7.58E-02	5.74E-03	4.513	4.589
	Ni1-O13	2	5.50E-03	7.58E-02	5.74E-03	4.751	4.827

Table S11: Fit parameter for Ni-dittmarite heated hydrothermally (100% H_2O) at T =90°C, R-factor= 0.008.

sample	scattering path	N	σ^2	R_{diff} [Å]	R_{diff}^2 [Å²]	R_{model} [Å]	R_{fit} [Å]
Ni 90°C, H_2O	Ni1-O1	**6.6(4)**	7.99E-03	2.22E-02	4.94E-04	2.043	2.066
$NH_4NiPO_4 \cdot H_2O$	Ni1-P1	1	2.50E-02	4.23E-02	1.79E-03	2.734	2.776
R-factor	Ni1-O2	2	1.02E-02	-1.91E-01	3.65E-02	3.283	3.092
0.008	Ni1-P2	3	2.50E-02	4.23E-02	1.79E-03	3.187	3.229
S_O^2 (err)	Ni1-P3	1	2.50E-02	4.23E-02	1.79E-03	3.274	3.316
2.5(4)	Ni1-O3	8	1.02E-02	-1.91E-01	3.65E-02	3.546	3.355
ΔE (err)	Ni1-Ni2	4	1.47E-02	-1.10E-01	1.20E-02	3.673	3.563
-0.8(4)	Ni1-O4	2	1.02E-02	-1.91E-01	3.65E-02	3.767	3.576
S_O^2 O1 (set)	Ni1-O5	8	1.02E-02	-1.91E-01	3.65E-02	3.878	3.687
0.91	Ni1-O6	4	1.47E-02	-1.10E-01	1.20E-02	3.800	3.690
	Ni1-O7	4	1.05E-02	-2.84E-01	8.07E-02	4.160	3.876
	Ni1-O8	4	1.47E-02	-1.10E-01	1.20E-02	4.111	4.001
	Ni1-O9	4	1.47E-02	-1.10E-01	1.20E-02	4.224	4.115
	Ni1-O10	1	1.05E-02	-2.84E-01	8.07E-02	4.498	4.214
	Ni1-O11	2	1.05E-02	-2.84E-01	8.07E-02	4.690	4.406
	Ni1-O12	2	1.05E-02	-2.84E-01	8.07E-02	4.733	4.449
	Ni1-Ni3	2	1.47E-02	-1.10E-01	1.20E-02	4.747	4.637
	Ni1-Ni4	1	1.47E-02	-1.10E-01	1.20E-02	4.831	4.721

Table S12: Fit parameter for Co-struvite at room temperature T = 25°C, R-factor= 0.014.

sample	scattering path	N	σ^2	R_{diff} [Å]	R_{diff}^2 [Å^2]	R_{model} [Å]	R_{fit} [Å]
Co-struvite (25°C)	Co1-O1	**6.4(5)**	0.008	2.65E-02	7.02E-04	2.058	2.084
$NH_4CoPO_4 \cdot 6H_2O$	Co1-H1	2	0.003	-1.09E-01	1.20E-02	2.616	2.506
R-factor	Co1-H2	2	0.003	3.15E-01	9.94E-02	2.211	2.527
0.014	Co1-H3	1	0.003	-1.09E-01	1.20E-02	2.686	2.577
S_O^2 (err)	Co1-H4	2	0.003	3.15E-01	9.94E-02	2.451	2.766
1.0(3)	Co1-H5	1	0.004	3.15E-01	9.94E-02	2.507	2.822
ΔE (err)	Co1-H6	4	0.004	3.15E-01	9.94E-02	2.549	2.865
3.2(7)	Co1-N1	1	0.004	-1.09E-01	1.20E-02	4.027	3.917
S_O^2 O1 (set)	Co1-N2	2	0.001	-1.09E-01	1.20E-02	4.133	4.023
0.9	Co1-O2	4	0.004	3.33E-01	1.11E-01	4.105	4.438
	Co1-P1	3	0.001	1.08E-01	1.17E-02	4.393	4.501
	Co1-O3	4	0.001	3.33E-01	1.11E-01	4.199	4.532
	Co1-O4	3	0.000	3.33E-01	1.11E-01	4.288	4.621
	Co1-O5	1	0.015	0.333	1.11E-01	4.362	4.694
	Co1-P2	2	0.015	0.108	1.17E-02	4.758	4.866
	Co1-O6	2	0.015	0.108	1.17E-02	4.826	4.934

Table S13: Fit parameter for Co-dittmarite T = 90°C, R-factor= 0.007.

sample	scattering path	N	σ^2	R_{diff} [Å]	R_{diff}^2 [Å^2]	R_{model} [Å]	R_{fit} [Å]
Co 90°C	Co1-O1	**6.0(4)**	0.003	-3.21E-02	1.03E-03	2.055	2.094
$NH_4CoPO_4 \cdot H_2O$	Co1-P1	1	0.012	1.50E-04	2.25E-08	2.797	2.791
R-factor	Co1-P2	2	0.012	1.50E-04	2.25E-08	3.209	3.203
0.007	Co1-P3	1	0.012	1.50E-04	2.25E-08	3.305	3.299
S_O^2 (err)	Co1-O2	2	0.014	3.08E-02	9.49E-04	3.313	3.322
1.6(4)	Co1-O3	2	0.014	3.08E-02	9.49E-04	3.592	3.601
ΔE (err)	Co1-Co2	4	0.013	-1.75E-02	3.06E-04	3.712	3.687
2.1(6)	Co1-O4	1	0.014	3.08E-02	9.49E-04	3.753	3.762
S_O^2 O1 (set)	Co1-O5	3	0.014	3.08E-02	9.49E-04	3.813	3.822
1.0	Co1-O6	1	0.014	3.08E-02	9.49E-04	3.944	3.953
	Co1-N1	1	0.013	-1.75E-02	3.06E-04	4.010	3.985
	Co1-O7	4	0.007	3.44E-01	1.18E-01	4.182	4.529
	Co1-Co3	2	0.013	-1.75E-02	3.06E-04	4.797	4.772
	Co1-O8	1	0.007	3.44E-01	1.18E-01	4.528	4.874
	Co1-O9	4	0.007	3.44E-01	1.18E-01	4.762	5.108

Table S14: Fit parameter for Co-dittmarite heated T = 150°C, R-factor= 0.011.

sample	scattering path	N	σ^2	R_{diff} [Å]	R_{diff}^2 [Å^2]	R_{model} [Å]	R_{fit} [Å]
Co 150°C	Co1-O1	**6.1(5)**	0.009	1.20E-02	1.43E-04	2.055	2.067
NH_4CoPO_4, am	Co1-P1	1	0.017	-4.22E-02	1.78E-03	2.797	2.755
R-factor	Co1-P2	2	0.017	-4.22E-02	1.78E-03	3.209	3.167
0.011	Co1-O2	4	0.022	-7.79E-02	6.07E-03	3.313	3.235
S_O^2 (err)	Co1-P3	1	0.017	-4.22E-02	1.78E-03	3.305	3.263
2.2(5)	Co1-O10-P4	1	0.022	4.34E-01	-6.56E-02	3.554	3.488
ΔE (err)	Co1-O3	4	0.022	-7.79E-02	6.07E-03	3.592	3.514
0.4(7)	Co1-Co2	4	0.022	-6.56E-02	4.31E-03	3.712	3.647
S_O^2 O1 (set)	Co1-O5	2	0.022	-7.79E-02	6.07E-03	3.753	3.675
0.85	Co1-O6	3	0.022	-7.79E-02	6.07E-03	3.813	3.735
	Co1-O7	1	0.022	-7.79E-02	6.07E-03	3.944	3.866
	Co1-O8	4	0.012	3.25E-01	1.06E-01	4.182	4.507
	Co1-Co9	2	0.022	-7.79E-02	6.07E-03	4.797	4.719
	Co1-O10	1	0.012	3.25E-01	1.06E-01	4.528	4.853
	Co1-O12	3	0.022	-7.79E-02	6.07E-03	4.949	4.871
	Co1-O13	4	0.012	3.25E-01	1.06E-01	4.762	5.087

Table S15: Fit parameter for HCPH an associated phases at T = 210°C, R-factor= 0.007.

sample	scattering path	N	σ^2	R_{diff} [Å]	R_{diff}^2 [Å^2]	R_{model} [Å]	R_{fit} [Å]
Co 210°C	Co1-O1	**5.1(3)**	0.007	-6.75E-02	4.56E-03	2.055	1.987
$HCoPO_4 \cdot H_2O$, NH_4CoPO_4, am, ($NH_4CoPO_4 \cdot H_2O$)	Co1-H1	1	0.018	-1.94E-01	3.78E-02	2.348	2.153
	Co1-H2	1	0.018	-1.94E-01	3.78E-02	2.758	2.564
	Co1-P1	1	0.038	-2.33E-01	5.44E-02	3.217	2.984
R-factor	Co1-Co2	2	0.018	-1.94E-01	3.78E-02	3.192	2.998
0.007	Co1-P2	2	0.038	-2.33E-01	5.44E-02	3.279	3.046
S_O^2 (err)	Co1-P3	1	0.038	-2.33E-01	5.44E-02	3.312	3.078
1.3(3)	Co1-P4	1	0.038	-2.33E-01	5.44E-02	3.413	3.179
ΔE (err)	Co1-O2	1	0.019	1.89E-01	3.56E-02	3.401	3.590
0.3(8)	Co1-O3	2	0.019	1.89E-01	3.56E-02	3.468	3.656
S_O^2 O1 (set)	Co1-O4	1	0.019	1.89E-01	3.56E-02	3.490	3.678
0.75	Co1-O5	1	0.019	1.89E-01	3.56E-02	3.621	3.810
	Co1-O6	1	0.019	1.89E-01	3.56E-02	3.821	4.009
	Co1-O7	1	0.019	1.89E-01	3.56E-02	3.871	4.060
	Co1-O8	1	0.019	1.89E-01	3.56E-02	4.095	4.284
	Co1-O9	1	0.019	1.89E-01	3.56E-02	4.147	4.335
	Co1-O10	3	0.019	1.89E-01	3.56E-02	4.203	4.391
	Co1-O11	3	0.019	1.89E-01	3.56E-02	4.346	4.535

Table S16: Fit parameter for ACP and associated phases at T = 240°C, R-factor=.

sample	scattering path	N	σ^2	R_{diff} [Å]	R_{diff}^2 [Å^2]	R_{model} [Å]	R_{fit} [Å]
Co 240°C	Co1-O1	**4.4(3)**	0.006	-7.69E-02	5.91E-03	2.055	1.978
NH_4CoPO_4, $HCoPO_4 \cdot H_2O$, amorphous	Co1-P1	2	0.020	-1.45E-01	2.11E-02	3.192	3.047
	Co1-P2	1	0.020	-1.45E-01	2.11E-02	3.217	3.072
	Co1-P3	2	0.020	-1.45E-01	2.11E-02	3.279	3.134
R-factor	Co1-P4	1	0.020	-1.45E-01	2.11E-02	3.312	3.166
0.011	Co1-O2	1	0.011	1.77E-01	3.15E-02	3.401	3.579
S_O^2 Amplitude	Co1-P5	1	0.020	-1.45E-01	2.11E-02	3.413	3.267
0.7(2)	Co1-O3	2	0.011	1.77E-01	3.15E-02	3.468	3.645
ΔE (err)	Co1-O4	1	0.011	1.77E-01	3.15E-02	3.490	3.667
1.0(6)	Co1-O5	1	0.011	1.77E-01	3.15E-02	3.621	3.799
S_O^2 O1 (set)	Co1-O6	1	0.011	1.77E-01	3.15E-02	3.821	3.998
0.75	Co1-O7	1	0.011	1.77E-01	3.15E-02	3.871	4.049
	Co1-O8	1	0.011	1.77E-01	3.15E-02	4.095	4.273
	Co1-O9	1	0.006	-7.69E-02	5.91E-03	4.147	4.070
	Co1-O10	3	0.014	9.33E-02	8.70E-03	4.203	4.296
	Co1-O11	3	0.014	9.33E-02	8.70E-03	4.346	4.440
	Co1-O12	2	0.014	9.33E-02	8.70E-03	4.410	4.503
	Co1-O13	1	0.014	9.33E-02	8.70E-03	4.456	4.550
	Co1-O14	2	0.014	9.33E-02	8.70E-03	4.504	4.597
	Co1-O15	1	0.014	9.33E-02	8.70E-03	4.580	4.673
	Co1-Co2	1	0.017	1.89E-01	3.57E-02	4.841	5.030
	Co1-O16	1	0.014	9.33E-02	8.70E-03	4.855	4.949
	Co1-P6	1	0.017	1.89E-01	3.57E-02	4.882	5.071
	Co1-O17	4	0.006	9.33E-02	8.70E-03	4.952	5.045
	Co1-O18	2	0.014	9.33E-02	8.70E-03	4.998	5.091
	Co1-Co3	2	0.017	1.89E-01	3.57E-02	5.147	5.336
	Co1-O19	1	0.017	1.89E-01	3.57E-02	5.187	5.376
	Co1-O20	1	0.006	1.89E-01	3.57E-02	5.288	5.477
	Co1-P7	1	0.017	1.89E-01	3.57E-02	5.321	5.510

Table S17: Fit parameter for ACP and associated phases at T = 270°C, R-factor=.

sample	scattering path	N	σ^2	R_{diff} [Å]	R_{diff}^2 [Å²]	R_{model} [Å]	R_{fit} [Å]
Co 270°C	Co1-O1	**3.7(2**	0.00	5.82E-02	3.39E-03	1.925	1.983
NH_4CoPO_4, $HCoPO_4 \cdot H_2O$, amorphous	Co1-P1	1	0.02	1.30E-01	1.70E-02	2.999	3.129
	Co1-P2	1	0.02	1.30E-01	1.70E-02	3.092	3.223
	Co1-P3	1	0.02	1.30E-01	1.70E-02	3.137	3.268
R-factor	Co1-O2	1	0.00	4.21E-01	1.77E-01	2.944	3.366
0.011	Co1-P4	1	0.02	1.30E-01	1.70E-02	3.277	3.407
S_O^2 (err)	Co1-O4	1	0.00	1.17E-01	1.38E-02	3.452	3.569
1.1(2)	Co1-O3	1	0.00	4.21E-01	1.77E-01	3.248	3.670
ΔE (err)	Co1-O5	1	0.00	1.17E-01	1.38E-02	3.645	3.763
1.1(5)	Co1-O6	1	0.00	1.17E-01	1.38E-02	3.691	3.809
S_O^2 O1 (set)	Co1-O7	1	0.00	1.17E-01	1.38E-02	3.814	3.931
0.75	Co1-O8	1	0.00	1.17E-01	1.38E-02	3.932	4.049
	Co1-Co2	2	0.01	-1.00E-	1.00E-04	4.318	4.308
	Co1-O10	1	0.00	1.17E-01	1.38E-02	4.269	4.386
	Co1-O11	1	0.00	1.17E-01	1.38E-02	4.324	4.441
	Co1-O12	1	0.00	1.17E-01	1.38E-02	4.370	4.487
	Co1-O9	1	0.00	4.21E-01	1.77E-01	4.152	4.573
	Co1-O13	1	0.00	1.17E-01	1.38E-02	4.911	5.028

Table S18: Fit parameter for ACP and amorphous phases at T = 300°C, R-factor= 0.010.

sample	scattering path	N	σ^2	R_{diff} [Å]	R_{diff}^2 [Å^2]	R_{model} [Å]	R_{fit} [Å]
Co 300°C	O1	**3.6(2)**	0.007	6.1E-03	3.71E-05	1.968	1.974
NH_4CoPO_4,	P1	2	0.030	-2.5E-01	6.31E-02	3.137	2.886
R-factor	P2	1	0.026	1.4E-01	1.92E-02	2.999	3.138
0.010	P3	1	0.026	1.4E-01	1.92E-02	3.092	3.231
S_O^2 (err)	P4	1	0.048	1.4E-01	1.86E-02	3.277	3.413
3.0(8)	O2	1	0.048	1.4E-01	1.86E-02	3.452	3.588
ΔE (err)	O3	1	0.048	1.4E-01	1.86E-02	3.645	3.781
-0.9(4)	O4	1	0.048	1.4E-01	1.86E-02	3.691	3.827
S_O^2 O1 (set)	O5	1	0.048	1.4E-01	1.86E-02	3.814	3.950
0.85	O6	1	0.041	-1.7E-01	2.99E-02	4.318	4.145
	O7	2	0.048	1.4E-01	1.86E-02	4.152	4.288
	O8	1	0.048	1.4E-01	1.86E-02	4.269	4.405
	O9	1	0.048	1.4E-01	1.86E-02	4.324	4.460
	O10	1	0.048	1.4E-01	1.86E-02	4.370	4.506
	O11	1	0.048	1.4E-01	1.86E-02	4.911	5.047
	O12	1	0.048	1.4E-01	1.86E-02	4.965	5.101

Table S19: Fit parameter for $Co_2P_2O_7$ with amorphous phases heated T = 400°C, t = 1d, R-factor= 0.005.

sample	scattering path	N	σ^2	R_{diff} [Å]	R_{diff}^2 [Å²]	R_{model} [Å]	R_{fit} [Å]
Co 400°C	Co1-O1	1	0.010	-4.58E-02	2.09E-03	2.076	2.030
$Co_2P_2O_7$, am	Co1-Co2	1	0.017	-1.96E-01	3.83E-02	3.155	2.959
R-factor	Co1-P1	1	0.042	-2.07E-01	4.27E-02	3.239	3.032
0.005	Co1-Co3	1	0.017	-1.96E-01	3.83E-02	3.249	3.053
S_O^2 (err)	Co1-Co4	1	0.017	-1.96E-01	3.83E-02	3.279	3.083
1.3(3)	Co1-P2	2	0.042	-2.07E-01	4.27E-02	3.295	3.088
ΔE (err)	Co1-P3	2	0.042	-2.07E-01	4.27E-02	3.326	3.119
-1.1(6)	Co1-O2	1	0.002	-9.34E-02	8.72E-03	3.271	3.178
S_O^2 O1 (set)	Co1-P4	1	0.042	-2.07E-01	4.27E-02	3.530	3.324
0.85	Co1-O3	1	0.002	-9.34E-02	8.72E-03	3.497	3.403
	Co1-O4	1	0.002	-9.34E-02	8.72E-03	3.579	3.486
	Co1-O5	1	0.002	-9.34E-02	8.72E-03	3.703	3.610
	Co1-O6	1	0.002	-9.34E-02	8.72E-03	3.758	3.665
	Co1-O7	3	0.037	-6.73E-02	4.53E-03	3.862	3.794
	Co1-O8	1	0.037	-6.73E-02	4.53E-03	3.929	3.862
	Co1-Co5	1	0.017	-1.96E-01	3.83E-02	4.123	3.927
	Co1-O9	2	0.037	-6.73E-02	4.53E-03	3.998	3.931
	Co1-P5	1	0.042	-2.07E-01	4.27E-02	4.153	3.946
	Co1-O10	2	0.037	-6.73E-02	4.53E-03	4.080	4.013
	Co1-P6	1	0.042	-2.07E-01	4.27E-02	4.290	4.084
	Co1-O10	2	0.037	-6.73E-02	4.53E-03	4.228	4.161
	Co1-O11	2	0.037	-6.73E-02	4.53E-03	4.371	4.303
	Co1-O12	1	0.037	-6.73E-02	4.53E-03	4.436	4.369
	Co1-O13	1	0.037	-6.73E-02	4.53E-03	4.475	4.408
	Co1-O14	3	0.037	-6.73E-02	4.53E-03	4.525	4.457
	Co1-O15	1	0.037	-6.73E-02	4.53E-03	4.554	4.487
	Co1-O16	2	0.037	-6.73E-02	4.53E-03	4.706	4.638
	Co1-O17	1	0.037	-6.73E-02	4.53E-03	4.733	4.666
	Co1-O18	1	0.037	-6.73E-02	4.53E-03	4.832	4.765
	Co1-P7	2	0.037	-6.73E-02	4.53E-03	4.865	4.798
	Co1-O19	1	0.037	-6.73E-02	4.53E-03	4.913	4.846
	Co1-Co6	1	0.037	-6.73E-02	4.53E-03	4.934	4.866
	Co1-Co7	1	0.037	-6.73E-02	4.53E-03	4.971	4.904
	Co1-Co8	1	0.037	-6.73E-02	4.53E-03	5.019	4.951
	Co1-O20	1	0.037	-6.73E-02	4.53E-03	5.208	5.141

Table S20: Fit parameter for $Co_2P_2O_7$ heated T = 800°C, t = 1d, R-factor= 0.015.

sample	scattering path	N	σ^2	R_{diff} [Å]	R_{diff}^2 [Å²]	R_{model} [Å]	R_{fit} [Å]
Co 800°C	Co1-O1	**5.6(3)**	0.010	-4.58E-02	2.09E-03	2.076	2.030
$Co_2P_2O_7$	Co1-Co2	1	0.017	-1.96E-01	3.83E-02	3.155	2.959
R-factor	Co1-P1	1	0.042	-2.07E-01	4.27E-02	3.239	3.032
0.015	Co1-Co3	1	0.017	-1.96E-01	3.83E-02	3.249	3.053
S_O^2 (err)	Co1-Co4	1	0.017	-1.96E-01	3.83E-02	3.279	3.083
2(2)	Co1-P2	2	0.042	-2.07E-01	4.27E-02	3.295	3.088
ΔE (err)	Co1-P3	2	0.042	-2.07E-01	4.27E-02	3.326	3.119
-1(1)	Co1-O2	1	0.002	-9.34E-02	8.72E-03	3.271	3.178
S_O^2 O1 (set)	Co1-P4	1	0.042	-2.07E-01	4.27E-02	3.530	3.324
0.85	Co1-O3	1	0.002	-9.34E-02	8.72E-03	3.497	3.403
	Co1-O4	1	0.002	-9.34E-02	8.72E-03	3.579	3.486
	Co1-O5	1	0.002	-9.34E-02	8.72E-03	3.703	3.610
	Co1-O6	1	0.002	-9.34E-02	8.72E-03	3.758	3.665
	Co1-O7	3	0.037	-6.73E-02	4.53E-03	3.862	3.794
	Co1-O8	1	0.037	-6.73E-02	4.53E-03	3.929	3.862
	Co1-Co5	1	0.017	-1.96E-01	3.83E-02	4.123	3.927
	Co1-O9	2	0.037	-6.73E-02	4.53E-03	3.998	3.931
	Co1-P6	1	0.042	-2.07E-01	4.27E-02	4.153	3.946
	Co1-O10	2	0.037	-6.73E-02	4.53E-03	4.080	4.013
	Co1-P7	1	0.042	-2.07E-01	4.27E-02	4.290	4.084
	Co1-O11	2	0.037	-6.73E-02	4.53E-03	4.228	4.161
	Co1-O12	2	0.037	-6.73E-02	4.53E-03	4.371	4.303
	Co1-O13	1	0.037	-6.73E-02	4.53E-03	4.436	4.369
	Co1-O14	1	0.037	-6.73E-02	4.53E-03	4.475	4.408
	Co1-O15	3	0.037	-6.73E-02	4.53E-03	4.525	4.457
	Co1-O16	1	0.037	-6.73E-02	4.53E-03	4.554	4.487
	Co1-O17	2	0.037	-6.73E-02	4.53E-03	4.706	4.638
	Co1-O18	1	0.037	-6.73E-02	4.53E-03	4.733	4.666
	Co1-O19	1	0.037	-6.73E-02	4.53E-03	4.832	4.765
	Co1-P6	2	0.037	-6.73E-02	4.53E-03	4.865	4.798
	Co1-O20	1	0.037	-6.73E-02	4.53E-03	4.913	4.846
	Co1-Co6	1	0.037	-6.73E-02	4.53E-03	4.934	4.866
	Co1-Co7	1	0.037	-6.73E-02	4.53E-03	4.971	4.904
	Co1-Co8	1	0.037	-6.73E-02	4.53E-03	5.019	4.951
	Co1-O21	1	0.037	-6.73E-02	4.53E-03	5.208	5.141

Table S21: Comparison of calculated degeneracies of Oxygens around the metal cation in the T-series

Chemical system	phase composition	T [°C]	degeneracy of Oxygen	Pre-peak Area App (err)
Ni	$NH_4NiPO_4 \cdot 6H_2O$	25	6.7(7)	0.025(1)
	amorphous	90	5.5(4)	0.032(1)
	amorphous	150	6.3(5)	0.030(1)
	amorphous	300	5.5(4)	0.034(2)
	amorphous	500	5.3(2)	0.036(1)
	amorphous	600	5.4(2)	0.041(2)
	$Ni_2P_2O_7$	800	5.6(3)	0.033(1)
	$NH_4NiPO_4 \cdot H_2O$	90 (H_2O)	6.6(4)	0.029(2)
Co	$NH_4CoPO_4 \cdot 6H_2O$	25	6.4(5)	0.026(1)
	$NH_4CoPO_4 \cdot H_2O$	90	6.0(4)	0.032(1)
	$NH_4CoPO_4 \cdot H_2O$	150	6.7(6)	0.041(2)
	NH_4CoPO_4, $HCoPO_4 \cdot H_2O$, amorphous	210	5.1(3)	0.071(1)
	NH_4CoPO_4, $HCoPO_4 \cdot H_2O$, amorphous	240	4.4(3)	0.077(3)
	NH_4CoPO_4, $HCoPO_4 \cdot H_2O$, amorphous	270	3.7(2)	0.078(3)
	NH_4CoPO_4, amorphous	300	3.6(2)	0.075(3)
	$Co_2P_2O_7$, amorphous	400	5.3(4)	0.048(1)
	$Co_2P_2O_7$	800	5.6(6)	0.033(1)

Table S22: summarized Proton conductivity data in variable temperatures and relative humidities (RH), -- no proton conductivity could be calculated.

thermal treated T [°C]	90°C, H2O	90°C	300°C	500°C	800°C	800°C
compound	NID	COD	ACP	amorphous	NPY	CPY
chemical formula	$NH_4NiPO_4 \cdot H_2O$	$NH_4CoPO_4 \cdot H_2O$	NH_4CoPO_4	($Ni\text{-}PO_4$)	$Ni_2P_2O_7$	$Co_2P_2O_7$
Measurement conditons	Variable RH at RT = 25°C, variable T at RH = 98%					
RH, RT	σ, conductivity [Scm^{-1}]					
68%	1.519E-07	1.542E-06	--	--	--	--
73%	2.787E-07	2.287E-06	--	--	--	--
78%	5.214E-07	3.913E-06	1.045E-07	--	--	--
83%	1.015E-06	7.752E-06	2.580E-07	--	--	--
88%	2.196E-06	1.933E-05	6.617E-07	8.490E-08	9.798E-08	--
93%	5.781E-06	4.486E-05	1.859E-06	2.430E-07	2.922E-07	1.23E-07
98%	4.220E-05	1.357E-04	7.479E-06	1.564E-06	3.443E-06	9.90E-07
Slope log(σ [S/cm]) vs. log(p_{H2O}, [atm])	16±2	13±1	18±1	35±7	2.1±0.4	8.8
25°C	4.228E-05	1.304E-04	7.485E-06	1.569E-06	3.443E-06	9.897E-07
30°C	5.691E-05	1.541E-04	9.430E-06	1.976E-06	5.907E-06	1.720E-06
40°C	8.851E-05	1.952E-04	1.508E-05	2.240E-06	5.938E-06	4.287E-06
50°C	1.352E-04	2.254E-04	2.014E-05	2.536E-06	6.127E-06	7.772E-06
60°C	1.656E-04	2.377E-04	2.923E-05	2.860E-06	6.897E-06	1.083E-05
70°C	2.364E-04	2.618E-04	3.994E-05	3.443E-06	7.409E-06	1.557E-05
80°C	3.495E-04	3.201E-04	6.422E-05	4.778E-06	8.914E-06	2.374E-05
Slope log(σ [S/cm]) vs. log(1000/T [K^{-1}])	-4.2±0.1	-1.9±0.1	-4.3±0.2	-1.7±0.1	-9.4±0.9	-5.7±0.4
Ea [eV/proton]	0.362	0.162	0.367	0.149	0.811	0.488
Ea [kJ/mole]	34.9	15.6	35.4	14.3	78.2	47.1

Table S23: Fit parameter of an equivalent circuit for Ni- and Co-dittmarite (T=90°C) in variable relative humidities (RH) and temperatures: R - resistance of resistor [Ω], P – pre-exponential factor of constant phase element (CPE), n – exponential factor [n = 1: pure capacitor, n = 0: pure resistor], W_S ,W_O- Warburg coefficients (Ohm s-0.5); -- =no error could be calculated.

sample	VH / VT	R [Ω]	Err %	P	Err %	n	Err %	W_S [$\Omega s^{-0.5}$]	Err %	W_O [$\Omega s^{-0.5}$]	Err %	W_S/W_O	Err %
Ni-dittmarite $NH_4NiPO_4 \cdot H_2O$	**68%**	579720	1	5.07E-10	5.7	0.77	0.7	236020	4.1	364880	5.4	**0.65**	**9.6**
	73%	317870	0.9	3.35E-10	4.6	0.81	0.5	116530	2.5	288350	5.8	**0.4**	**8.3**
	78%	170060	1.1	2.79E-10	6.5	0.84	0.6	65981	3.5	140130	7	**0.47**	**10.5**
	83%	85712	1.3	2.23E-10	8.1	0.86	0.7	51261	6	47823	5.4	**1.07**	**11.4**
	88%	40077	1.1	2.73E-10	7.1	0.85	0.6	25303	5.9	21439	4.5	**1.18**	**10.4**
	93%	15539	0.8	4.71E-10	6.3	0.82	0.5	10103	4.2	8868	3.3	**1.14**	**7.5**
	98%	2794	0.7	4.36E-11	10	0.98	0.7	4153	4	1842	1.6	**2.25**	**5.7**
	25°C	2159	0.4	2.34E-10	7.5	0.87	0.5	955	1	4541	5	**0.21**	**6**
	30°C	1609	0.5	1.86E-10	3	0.88	0.8	752	1.2	2396	4.2	**0.31**	**5.4**
	40°C	1035	0.5	1.12E-10	9	0.92	1	513	1.2	919	3	**0.56**	**4.2**
	50°C	679	0.5	3.47E-09	6	0.77	4.9	404	1.3	488	2.5	**0.83**	**3.8**
	60°C	558	0.6	6.93E-07	7	0.81	10.8	337	1.5	292	2.4	**1.16**	**3.9**
	70°C	388	0.6	2.44E-09	8	0.85	4.2	267	1.5	184	2.3	**1.45**	**3.8**
	80°C	264	0.8	3.92E-07	8	0.83	9.1	250	1.9	109	2	**2.31**	**3.9**
Co-dittmarite $NH_4CoPO_4 \cdot H_2O$	**68%**	126860	0.5	9.03E-11	2.9	0.92	0.3	9.85E-13	--	439	67.6	**0**	**--**
	73%	86063	0.6	8.35E-11	3.3	0.93	0.3	8.94E-14	--	499	66.2	**0**	**--**
	78%	50120	0.4	9.55E-11	4	0.93	0.3	1.21E-12	--	537	47.1	**0**	**--**
	83%	25151	0.5	1.17E-10	3.2	0.91	0.3	1259	13	734	11	**1.72**	**23.9**
	88%	10056	0.5	2.87E-10	4.1	0.85	0.3	1314	10.6	464	10.1	**2.83**	**20.7**
	93%	4352	0.4	4.32E-11	4.5	0.98	0.3	1303	11	280	4.8	**4.66**	**15.8**
	98%	1452	0.7	1.13E-10	5.5	0.89	2.1	1280	10.1	199	4.3	**6.45**	**14.4**
	25°C	1500	0.6	6.44E-11	6.3	0.96	0.7	1558	2	308	1.4	**5.06**	**3.4**
	30°C	1274	0.6	4.91E-11	7.1	0.98	0.6	1347	1.8	246	1.4	**5.47**	**3.2**
	40°C	1006	0.6	3.65E-11	7.9	1	1	1089	2	201	1.6	**5.41**	**3.6**
	50°C	870	0.5	5.11E-10	4	0.82	4.7	981	2.5	178	1.8	**5.51**	**4.3**
	60°C	819	0.6	8.45E-11	5	0.95	3.9	901	2.6	166	1.6	**5.44**	**4.1**
	70°C	748	0.5	1.13E-10	6	0.92	3.8	860	2.4	139	1.3	**6.2**	**3.7**
	80°C	610	0.5	4.28E-10	6	0.82	9.3	818	2.1	121	1.1	**6.73**	**3.2**

Table S24: Proton conductivity data of selective transition metal phosphate compounds reported in literature; o.w. = our work.

material	*chemical composition*	*T [°C]/ RH [%]*	*σ [S/cm]*	*E_a (eV)*	*Ref.*
ionomer	NAFION®	25/98	$7.80*10^{-2}$	-	6, 7
Ba-Nd-Ca-Sc-oxide	$BaNd_{0.8}Ca_{0.2}ScO_{3.9}$	900/-	$2.10*10^{-4}$		8
Ba-Nd-Ca-Sc-oxide	$BaNd_{0.8}Ca_{0.2}ScO_{3.9}$	800/-	$3.10*10^{-4}$		8
Ba-Nd-Sc-oxide	$BaNdScO_4$	800/-	$1.10*10^{-2}$		8
Ba-Er-Al-Zr-oxide	$Ba_5Er_2Al_2ZrO_{13}$	300-1200/-	$> 10^{-3}$	0.58-1.17	9
La-Nb-oxide	$LaNbO_4$	950/2% H_2O	$\approx 10^{-3}$	-	10
Sr-Gd-Ga-oxides	$Gd_{2.9}Sr_{0.1}GaO_{5.95}$	600°C/wet Ar	10^{-3}		11
Ba-La-In-oxide	$BaLaInO_4$	400°C/humidified air	$2*10^{-7}$	-	12
Ba-In-oxides	$Ba_2In_2O_5$	300°C/humidified air	$1.3*10^{-6}$	0.6	13
Sr-vanadates	$Sr_3V_2O_8$	600°C/humidified air	$1.0*10^{-4}$		14
Na-Al-PO_4	$Na_6[(AlPO_4)_8(OH)_6]\cdot 9H_2O$	20/98	$3.60*10^{-3}$	0.21	15
Al-PO_4	amorphous				
doped $Sn_2P_2O_7$	$In_{0.1}Sn_{0.9}P_2O_7$	300/-	0.195	-	16
Sn-PO_4	$Sn(HPO_4)_2$ $3H_2O$	100/-	$1.00*10^{-2}$	-	17
ZrP_2O_7	$Zr(P_2O_7)_{0.81}(O_3POH)_{0.38}$	20/98	$1.30*10^{-3}$	-	18
Sn-PO4	-	30/90	$1.35*10^{-4}$	5.52	19
Zr-PO4	-	30/90	$1.25*10^{-4}$	0.24	
Sn-Zr-PO4	-	30/90	$1.47*10^{-4}$	5.50	
TiP_2O_7	TiP_2O_7	100/-	$4.40*10^{-3}$	0.14	20
Ti-PO_4	$Ti_2(HPO_4)_4$	20/95	$1.20*10^{-3}$	0.13	21
org./inorg. Mn-PO_4-comp.	$(C_2H_{10}N_2)$ $[Mn_2(HPO_4)_3](H_2O)$	20/99	$1.60*10^{-3}$	0.22	22
org./inorg. Mn-PO_4-comp.	$(C_2H_{10}N_2)$ $[Mn_2(PO_4)_2]$ $2H_2O$	20/99	$7.00*10^{-3}$	0.22	22
org./inorg. Fe-PO_4-comp.	$(NH_3(CH_2)_3NH_3)_2[Fe_4(OH)_3(HPO_4)_2(PO_4)_3]$ $4H_2O$	40/H_2O-NH_3 vapour	$5.00*10^{-2}$	-	23
org./inorg. Fe-PO_4-comp.	$(C_4H_{12}N_2)_{1.5}[Fe_2(OH)(H_2PO_4)(HPO_4)_2(PO_4)]$ $0.5(H_2O)$	40/98	$5.10*10^{-4}$	-	24
Fe-PO_4-comp.	$(C_4H_{12}N_2)_{1.5}[Fe_2(OH)(H_2PO_4)(HPO_4)_2(PO_4)]$ $0.5(H_2O)$	40/98	$5.10*10^{-4}$	-	24
org./inorg. Co-PO_4-comp.	$(C_2N_2H_{10})_{0.5}CoPO_4$	56/98	$2.00*10^{-3}$	1.01	25
org./inorg. Zn-PO4-comp.	$NMe_4Zn[HPO_4][H_2PO_4]$	30/98	$1.30*10^{-2}$	0.92	26
K-V-PO_4	$K_2[(VO)_2(HPO_4)_2(C_2O_4)]$	40/95	$1.15*10^{-2}$	-	27
NH_4-Ni -PO_4	NH_4NiPO_4 H_2O	25/98	$4.20*10^{-5}$	0.36	o.w.
NH_4-Co-PO_4	NH_4NiPO_4 H_2O	25/98	$1.40*10^{-4}$	0.16	o.w.

References

1. W. Görner, M. P. Hentschel, B. R. Müller, H. Riesemeier, M. Krumrey, G. Ulm, W. Diete, U. Klein and R. Frahm, BAMline: the first hard X-ray beamline at BESSY II, *Nuclear Instruments and Methods in Physics Research A*, 2001, **467-468**, 703-706.
2. B. Ravel and M. Newville, ATHENA, ARTEMIS, HEPHAESTUS: data analysis for X-ray absorption spectroscopy using IFEFFIT, *J Synchrotron Radiat*, 2005, **12**, 537-541.
3. G. A. Ragoisha and A. S. Bondarenko, Potentiodynamic electrochemical impedance spectroscopy, *Electrochimica Acta*, 2005, **50**, 1553-1563.
4. L. Popovi, D. de Waal and J. C. A. Boeyens, Correlation between Raman wavenumbers and P-O bond lengths in crystalline inorganic phosphates, *Journal of Raman Spectroscopy*, 2005, **36**, 2-11.
5. K. D. Litasov and N. M. Podgornykh, Raman spectroscopy of various phosphate minerals and occurrence of tuite in the Elga IIE iron meteorite, *Journal of Raman Spectroscopy*, 2017, **48**, 1518-1527.
6. Y. Sone, P. Ekdunge and D. Simonsson, Proton Conductivity of Nafion 117 as Measured by a Four-Electrode AC Impedance Method, *Journal of The Electrochemical Society*, 1996, **143**, 1254.
7. Y. Sone, P. Ekdunge and D. Simonsson, Proton Conductivity of Nafion 117 as Measured by a Four-Electrode AC Impedance Method, *Journal of The Electrochemical Society*, 2019, **143**, 1254-1259.
8. M. Shiraiwa, T. Kido, K. Fujii and M. Yashima, High-temperature proton conductors based on the (110) layered perovskite BaNdScO4, *Journal of Materials Chemistry A*, 2021, **9**, 8607-8619.
9. T. Murakami, J. R. Hester and M. Yashima, High Proton Conductivity in Ba5Er2Al2ZrO13, a Hexagonal Perovskite-Related Oxide with Intrinsically Oxygen-Deficient Layers, *Journal of the American Chemical Society*, 2020, **142**, 11653-11657.
10. R. Haugsrud and T. Norby, High-temperature proton conductivity in acceptor-doped LaNbO4, *Solid State Ionics*, 2006, **177**, 1129-1135.
11. A. Iakovleva, A. Chesnaud, I. Animitsa and G. Dezanneau, Insight into the synthesis and electrical properties of alkali-earth-substituted Gd3GaO6 oxide-ion and proton conductors, *International Journal of Hydrogen Energy*, 2016, **41**, 14941-14951.
12. N. Tarasova, I. Animitsa and A. Galisheva, Effect of doping on the local structure of new block-layered proton conductors based on BaLaInO4, *Journal of Raman Spectroscopy*, 2020, **51**, 2290-2297.
13. G. B. Zhang and D. M. Smyth, Protonic conduction in Ba2In2O5, *Solid State Ionics*, 1995, **82**, 153-160.
14. S. Fop, J. A. Dawson, D. N. Tawse, M. G. Skellern, J. M. S. Skakle and A. C. McLaughlin, Proton and Oxide Ion Conductivity in Palmierite Oxides, *Chemistry of Materials*, 2022, **34**, 8190-8197.
15. Y. Sun, Y. Yan, Y. Wang, Y. Li, J. Li and J. Yu, High proton conduction in a new alkali metal-templated open-framework aluminophosphate, *Chemical Communications*, 2015, **51**, 9317-9319.
16. K. Scott, C. Xu and X. Wu, Intermediate temperature proton-conducting membrane electrolytes for fuel cells, *WIREs Energy and Environment*, 2014, **3**, 24-41.
17. W. Huang, S. Komarneni, Y. D. Noh, J. Ma, K. Chen, D. Xue, X. Xue and B. Jiang, Novel inorganic tin phosphate gel: multifunctional material, *Chem Commun (Camb)*, 2018, **54**, 2682-2685.
18. G. Alberti, M. Casciola, S. Cavalaglio and R. Vivani, Proton conductivity of mesoporous zirconium phosphate pyrophosphate, *Solid State Ionics*, 1999, **125**, 91-97.
19. P. V. Valsaraj and C. Janardanan, Comparative studies on Proton conducting nature of Copper selective tin

Zirconium phosphate Cation exchanger with its single Salts counter parts, *Research Journal of Chemical Sciences*, 2014, **4**, 84-90.

20. W. H. J. Hogarth, S. S. Muir, A. K. Whittaker, J. C. Diniz da Costa, J. Drennan and G. Q. Lu, Proton conduction mechanism and the stability of sol–gel titanium phosphates, *Solid State Ionics*, 2007, **177**, 3389-3394.
21. P. G. M. Mileo, T. Kundu, R. Semino, V. Benoit, N. Steunou, P. L. Llewellyn, C. Serre, G. Maurin and S. Devautour-Vinot, Highly Efficient Proton Conduction in a Three-Dimensional Titanium Hydrogen Phosphate, *Chemistry of Materials*, 2017, **29**, 7263-7271.
22. H.-R. Zhao, C. Xue, C.-P. Li, K.-M. Zhang, H.-B. Luo, S.-X. Liu and X.-M. Ren, A Two-Dimensional Inorganic–Organic Hybrid Solid of Manganese(II) Hydrogenophosphate Showing High Proton Conductivity at Room Temperature, *Inorganic Chemistry*, 2016, **55**, 8971-8975.
23. H.-r. Zhao, Y. Jia, Y. Gu, F.-y. He, K.-m. Zhang, Z.-f. Tian and J.-L. Liu, A 3D open-framework iron hydrogenophosphate showing high proton conductance under water and aqua-ammonia vapor, *RSC Advances*, 2020, **10**, 9046-9051.
24. K.-m. Zhang, Y.-l. Lou, F.-y. He, H.-b. Duan, X.-q. Huang, Y. Fan and H.-r. Zhao, The water-mediated proton conductivity of a 1D open framework inorganic-organic hybrid iron phosphate and its composite membranes, *Inorganic Chemistry Communications*, 2021, **134**, 109032.
25. M. Wang, H.-B. Luo, S.-X. Liu, Y. Zou, Z.-F. Tian, L. Li, J.-L. Liu and X.-M. Ren, Water assisted high proton conductance in a highly thermally stable and superior water-stable open-framework cobalt phosphate, *Dalton Transactions*, 2016, **45**, 19466-19472.
26. J.-W. Yu, H.-J. Yu, Q. Ren, J. Zhang, Y. Zou, H.-B. Luo, L. Wang and X.-M. Ren, Humidity-sensitive irreversible phase transformation of open-framework zinc phosphate and its water-assisted high proton conduction properties, *Dalton Transactions*, 2021, **50**, 8070-8075.
27. H.-X. Sun, H.-N. Wang, Y.-H. Zou and X. Meng, Tuning proton conduction by different particle sizes in open-framework metal phosphates, *Inorganic Chemistry Communications*, 2021, **124**, 108322.